Orbitally Excited Charm Mesons produced in Semileptonic B-decay

Cand. Scient. Thesis in Experimental Particle Physics

Anne-Kari Ytrestøl

Department of Physics
University of Oslo

May 3, 1998

Abstract

2.2 million hadronic Z^0 decays recorded by the DELPHI detector at LEP in 1994 and 1995 have been analysed in order to study semileptonic B-decays into narrow orbitally excited D-mesons, D_J^0. The D_J^0 is reconstructed in the mode $D^*(D^0\pi)\pi$ with $D^0 \to K\pi$. A clear D^* signal is seen. A signal of 16 events is observed for $D_J{}^0$ and the branching ratio of this decay was measured to be

$$Br(B^- \to D_J^0(D^{*+}\pi^-)\ell^-\bar{\nu_\ell}) = \underline{(\,1.6 \pm 0.9\,)\,\%} \quad \text{(preliminary)}$$

An estimate of the upper limit of the branching ratio gives

$$Br(B^- \to D_J^0(D^{*+}\pi^-)\ell^-\bar{\nu_\ell}) \; < \underline{3.0\,\%,\ (95\%\,\text{C.L.})} \quad \text{(preliminary)}$$

Preface

The thesis has been written for the Cand. Scient. degree in physics at the University of Oslo. Since I started the work I have had an opportunity to learn how experimental work is done, and especially how it is done in a particle physics experiment. During my study I have had the chance to go to CERN several times, which has been both useful and inspiring. It has been a positive experience to have contact with people in DELPHI working in the same field as I.

I would like to thank my parents, Kirsti, Mikkel and my friends for their support, and the other students in the High Energy Physics group for making this a great environment to study in. Thanks a lot to my supervisor, Torleiv Buran, who introduced me to this exciting branch of physics, and who has always been a great support. Special thanks to Anders Westreng Borgland and Ole Myren Røhne, and also to Lucia Di Ciaccio, Michael Feindt and Guennadi Borisov for the help they have given me at CERN.

Oslo, May 3, 1998
Anne-Kari Ytrestøl

Contents

1 Introduction

In order to measure the V_{cb}-element of the CKM-matrix, which is related to the probability for a b-quark to decay weakly to a c-quark, the semileptonic B-decay $B \to \overline{D}^{*} \ell^{+}\nu_{\ell}$ is well suited. Heavy Quark Effective Theory (HQET) predicts that the rate for this process when the D^{*} is produced at rest is a function of $\mid V_{cb} \mid^{2}$ [7].

Not all semileptonic decays of B-mesons to D-mesons are accounted for by the decays $B \to D\ell\bar{\nu_{\ell}}$ and $B \to D^{*}\ell\bar{\nu_{\ell}}$, some decay to orbitally excited D-mesons $B \to D^{**}\ell\bar{\nu_{\ell}}$. which may subsequently decay to $D^{*}\pi$ and thus be an important background of $B \to \overline{D}^{*} \ell^{+}\nu_{\ell}$.

HQET predicts the existence of four orbitally excited D-mesons with orbital angular momentum L=1, two narrow and two broad states, where the latter cannot be seen experimentally. The narrow states have been previously observed [7, 20].

Measurement of the branching ratio of $B \to D^{**}\ell\bar{\nu_{\ell}}$ is thus important in order to test the HQET predictions, as well as give a better determination of the branching ratio of $B \to \overline{D}^{*} \ell^{+}\nu_{\ell}$.

In the present analysis neutral D^{**} mesons have been reconstructed from their subsequent decay into $D^{*}\pi$, where D^{*} decays into $D^{0}\pi$. The D^{0} is reconstructed in the mode with $K^{-}\pi^{+}$ in the final state. A clear signal corresponding to D^{*} together with a signal due to D^{**} is seen.

The thesis begins with an outline of the theoretical background of the analysis (chapter 2 & 3). This is followed by a description of the DELPHI experiment (chapter 4) and the criteria of how and why events were selected for analysis (chapter 5). The results of the selection are shown (chapter 6), followed by a discussion of the results and the conclusion (chapter 7 & 8).

2 Theoretical background

The following chapter gives an introduction to particle physics and offers an explanation to why the study of orbitally excited D-mesons is important.

2.1 Introduction to particle physics and the Standard Model

An elementary particle is a particle which cannot be divided into smaller constituents. The first to be discovered was the electron which was discovered in 1897 by J. J. Thompson. He observed that cathode rays are beams of particles; namely electrons [1].

The electron is a charged particle and thus experiences *the electromagnetic force*. According to quantum field theory, all interactions are the results of particle exchanges, and these force-carrying particles are called *gauge-bosons*. In the electromagnetic case, the photon, the quantum of the electromagnetic field, is the carrier of the force. Quantum Electro Dynamics (QED), developed in the 1930s, is the theory for the quantized and relativistically covariant description of the electromagnetic interaction [2]. Richard P. Feynman represented interactions by using diagrams, see Figure 1 [3].

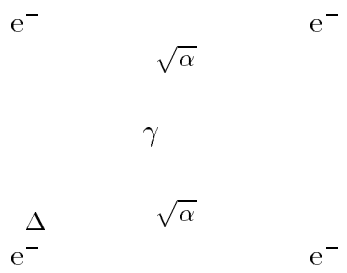

Figure 1: Feynman diagram representing electrons interacting by photon exchange. The probability for emitting a photon is proportional to α.

The probability for electron emission or absorption of a photon is called the strength of the interaction and is proportional to

$$\alpha = \frac{e^2}{4\pi} \tag{1}$$

where e is the elementary charge[1]. α is called the coupling constant, and a

[1]The rationalized Heaviside-Lorentz system of electromagnetic units is used along with natural units [2]. Natural units (nu) are frequently used in particle physics. In natural units

$$\hbar = c = 1$$

Using nu, all physical quantities have the dimension of a power of energy, i.e. the dimension of mass, momentum and energy are the same [4].

factor $\sqrt{\alpha}$ arises for every emitted or absorbed photon, i.e. for each vertex in Figure 1. Figure 1 is a diagram of lowest order, which corresponds to the diagram with the lowest number of vertices, for electron-electron scattering. Corrections arise due to higher-order diagrams, for example the photon self-energy where the photon fluctuates into an electron-positron pair, see Figure 2 [3].

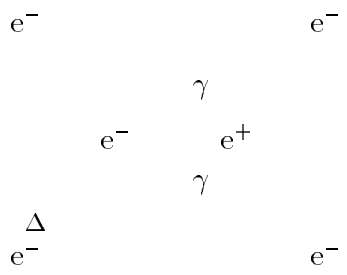

Figure 2: Feynman diagram which shows the photon self-energy diagram.

Since the discovery of the neutron in 1932 it was known that the constituents of the atom were electrons, protons and neutrons. Protons and neutrons were assumed to be elementary particles [1]. However scattering experiments performed in the 1960s indicated point-like particles inside the proton, and in 1964 Murray Gell-Mann and George Zweig independently developed the *quark* model [1]. Surprisingly, the quarks have charges of $+\frac{2}{3}$e and $-\frac{1}{3}$e and it was predicted that the proton contained two u-quarks (charge $+\frac{2}{3}$e) and one d-quark (charge $-\frac{1}{3}$e), giving an overall charge +1e for the proton. Both protons and neutrons are made of three quarks. Generally particles made of three quarks are referred to as *baryons* while particles consisting of one quark and one antiquark are called *mesons*. Particles which consist of quarks are called *hadrons*, and quark combinations other than (qqq) for baryons and ($q\bar{q}$) for mesons are not known.

Discoveries of a wide range of baryons and mesons implied that there had to be more than two quarks. In fact six different quarks (or quark *flavours*) have been discovered: up(u) and down(d), charm(c) and strange(s), bottom or beauty(b) and top(t). The quark masses vary in the range from a few MeV/c^2 (the u and d-quarks) to $\sim$180 GeV/c^2, which is the top-quark mass. In addition to electric charge quarks also carry a *colour* charge. The property of colour had to be assigned [4] to the quarks in order for them to obey the Pauli exclusion principle, which states that only one fermion, i.e. a particle with half-integer intrinsic spin s=n$\cdot\frac{1}{2}$, is allowed in each quantum state [5, 6].

Each quark may appear in three different colours. In the same way as the electromagnetic interaction originates from electric charge, the origin of the

strong interaction is the colour charge. Therefore only particles with colour charge may interact through the strong force, and the related gauge bosons are called *gluons*. They are electrically neutral and massless and they carry a colour charge just like the quarks. The name strong interaction originates from the fact that the coupling constant α_s of the interaction becomes larger for larger separations between strongly interacting particles, more on this in section 2.3. In fact quarks are so strongly bound inside hadrons that free quarks never have been observed. The strong interaction is described by Quantum Chromo Dynamics, QCD.

In 1953 another elementary particle was discovered, the *neutrino*, which had already been predicted by Wolfgang Pauli in 1931 [1]. The neutrino is a spin-$\frac{1}{2}$ fermion and has neither electric charge nor colour charge. Its mass is very small, perhaps even zero, and it rarely interacts with matter [7]. For massless neutrinos the Dirac equation which is the Lorentz covariant equation describing fermions [3], gives two different solutions: a left-handed neutrino (i.e. with helicity λ = -$\frac{1}{2}$) and a right-handed antineutrino ($\lambda = +\frac{1}{2}$). Such a wave equation is not invariant under the parity operation since it would result in $\nu_L \rightarrow \nu_R$, more on this in section 2.2.1. Neutrinos interact through the weak interaction, another fundamental force which was discovered in nuclear β-decay. The Lagrangian of the weak interaction has the form $\bar{\psi}\gamma^\mu$ $\frac{1}{2}(1 - \gamma^5)\psi$. The mixture of vector ($\bar{\psi}\gamma^\mu\psi$) and axial vector ($\bar{\psi}\gamma^\mu\gamma^5\psi$) leads to parity violation. The term $\frac{1}{2}(1 - \gamma^5)$ projects out only ν_L in agreement with experiments [2].

The weak interaction differs from the electromagnetic and the strong interaction as the mediators of the weak force are massive particles. There are three associated gauge bosons: W^+, W^- and Z^0. Both *leptons*[2] and quarks experience the weak force. The weak interaction can change one quark flavour or lepton flavour into another, for instance a u- to a d-quark or an electron to a neutrino, by W^+ or W^- exchange, Figure 3(a). This kind of weak interaction is called a flavour changing charged current, while Z^0 exchange is called a weak neutral current, since it does not change the flavour of the quark or lepton, Figure 3(b).

When the Feynman-diagrams for Z^0-exchange Figure 3(b) and the diagram for the electromagnetic interaction in Figure 1 are compared, they look very similar. Indeed it turns out that the electromagnetic and the weak force are two manifestations of the same interaction. The unification of the electromagnetic and the weak interaction to an electroweak field theory was

[2]Leptons are spin-$\frac{1}{2}$ fermions without strong interactions. The six discovered leptons are the electron and its two heavier sisters, the muon (discovered 1936) and the tauon (discovered 1975) and three neutrinos, one associated with each charged lepton.

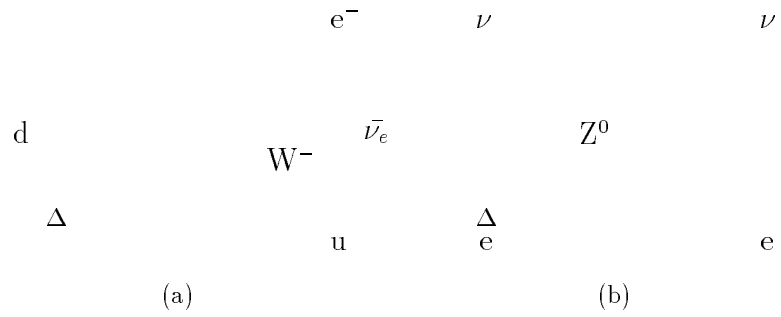

Figure 3: Feynman diagrams of weak interactions. (a) shows the process of turning a d-quark into a u-quark, and the emission of an electron and an electron-antineutrino. This is what take place when a neutron decays. (b) shows neutrino-electron elastic scattering.

done by Glashow, Weinberg and Salam in the 1960s [2].

In Table I [7] an overview of the known elementary particles is given. There are six quarks, six leptons, (and their corresponding antiparticles, which are not shown) and the gauge bosons. In addition the existence of Higgs bosons is predicted. They are gauge bosons necessary to explain particle masses, but they have not yet been observed.

As indicated in Table I quarks and leptons can be grouped together in generations, where

$$\begin{pmatrix} u \\ d \end{pmatrix} \quad \begin{pmatrix} e \\ \nu_e \end{pmatrix} \tag{2}$$

is the first generation.

The joint theory which describes quarks, leptons and their anti-particles, and the gauge bosons is called the Standard Model.

2.2 Weak interactions

The weak interaction Lagrangian of the flavour-changing charged current is given by [2]

$$\begin{aligned} \mathcal{L}_{int} &= -\frac{g}{\sqrt{2}} \{(\bar{\nu}_e, \bar{\nu}_\mu, \bar{\nu}_\tau)\gamma^\mu V_{CKM} \begin{pmatrix} e_L \\ \mu_L \\ \tau_L \end{pmatrix} + \\ &\quad (\bar{u}_L, \bar{c}_L, \bar{t}_L)\gamma^\mu V_{CKM} \begin{pmatrix} d_L \\ s_L \\ b_L \end{pmatrix} \} W_\mu^\dagger + \text{h.c.} \end{aligned} \tag{3}$$

Table I: An overview of the Standard Model quarks, leptons and gauge bosons.

	Name	Spin	Electric Charge	Mass (GeV/c^2)
Quarks	u (up)	$\frac{1}{2}$	$+\frac{2}{3}$	2 - 8 $\times 10^{-3}$
	d (down)	$\frac{1}{2}$	$-\frac{1}{3}$	5 - 15 $\times 10^{-3}$
	c (charm)	$\frac{1}{2}$	$+\frac{2}{3}$	1.0 - 1.6
	s (strange)	$\frac{1}{2}$	$-\frac{1}{3}$	0.1 - 0.3
	t (top)	$\frac{1}{2}$	$+\frac{2}{3}$	180
	b (bottom)	$\frac{1}{2}$	$-\frac{1}{3}$	4.1 - 4.5
Leptons	e (electron)	$\frac{1}{2}$	-1	0.511 $\times 10^{-3}$
	ν_e (e-neutrino)	$\frac{1}{2}$	0	< 10 - 15 eV/c^2
	μ (muon)	$\frac{1}{2}$	-1	105,7 $\times 10^{-3}$
	ν_μ (μ-neutrino)	$\frac{1}{2}$	0	< 0.17 MeV/c^2
	τ (tauon)	$\frac{1}{2}$	-1	1.777
	ν_τ (τ-neutrino)	$\frac{1}{2}$	0	< 24 MeV/c^2
Gauge Bosons	γ (photon)	1	0	0
	gluon	1	0	0
	$W^\pm$	1	± 1	80.3
	Z^0	1	0	91.18

where g is a coupling constant and the subscript $_L$ refers to left-handed. V_{CKM} is the Cabibbo-Kobayashi-Maskawa mixing matrix:

$$V_{CKM} = \begin{pmatrix} V_{ud} & V_{us} & V_{ub} \\ V_{cd} & V_{cs} & V_{cb} \\ V_{td} & V_{ts} & V_{tb} \end{pmatrix} \tag{4}$$

The mass eigenstates q of the quark fields:

$$\begin{pmatrix} u \\ d \end{pmatrix} \quad \begin{pmatrix} c \\ s \end{pmatrix} \quad \begin{pmatrix} t \\ b \end{pmatrix} \tag{5}$$

are not identical to the eigenstates q′ of the weak interaction:

$$\begin{pmatrix} u \\ d' \end{pmatrix} \quad \begin{pmatrix} c \\ s' \end{pmatrix} \quad \begin{pmatrix} t \\ b' \end{pmatrix} \tag{6}$$

The Cabibbo-Kobayashi-Maskawa mixing matrix relates q and q′ to each other. In the case of only two quark generations the mixing matrix becomes

a 2×2 matrix which can be parametrized by one angle, the Cabibbo-angle θ_C:

$$V = \begin{pmatrix} \cos\theta_C & \sin\theta_C \\ -\sin\theta_C & \cos\theta_C \end{pmatrix} \tag{7}$$

giving

$$d' = d\cos\theta_C + s\sin\theta_C \tag{8}$$
$$s' = -d\sin\theta_C + s\cos\theta_C \tag{9}$$

This means that the states participating in weak interactions are a mixture of two quark mass eigenstates, which allows processes otherwise forbidden to occur [4]. Considering all three generations the matrix can be parametrized using three angles θ_1, θ_2, θ_3 and a complex phase factor $e^{i\delta}$ [4, 7].

2.2.1 Symmetries and CP-violation

Symmetries are important in physics. For instance the invariance of the Hamiltonian under the translation

$$\mathbf{x}_i \longrightarrow \mathbf{x}_i' = \mathbf{x}_i + \mathbf{a} \tag{10}$$

leads to conservation of momentum, i.e. $[\hat{\mathbf{p}}, \mathrm{H}]=0$ [4]. Another symmetry is parity. The parity operator is defined by

$$\hat{P}\Psi(\mathbf{x}, t) \equiv P_a\Psi(-\mathbf{x}, t) \tag{11}$$

where P_a is a constant phase factor:

$$\hat{P}^2\Psi(\mathbf{x}, t) = P_a^2\Psi(\mathbf{x}, t) \Rightarrow P_a = \pm 1 \tag{12}$$

The parity of a system is conserved if its Hamiltonian is unchanged, i.e.

$$H(\mathbf{x}_1', \mathbf{x}_2', ...) = H(-\mathbf{x}_1, -\mathbf{x}_2, ...) = H(\mathbf{x}_1, \mathbf{x}_2, ...) \tag{13}$$

This turns out to be the case for both the electromagnetic and the strong interaction, but is violated by the weak interaction. The same applies for charge conjugation, the operator which replaces particles with their corresponding antiparticles:

$$\hat{C}|a\Psi\rangle = |\bar{a}\Psi\rangle \tag{14}$$

Until CP-violation was discovered in neutral kaon decay in 1964 [4], the combined operation of Parity and Charge Conjugation operators, CP, was

assumed a conserved quantity in all systems, but it is also violated by the weak interaction. CP conservation means that there is a symmetry between matter and antimatter,but due to CP-violation the symmetry is broken.

The complex phase in the CKM-matrix is needed to explain CP violation in the Standard Model. Experimental knowledge of the values of the elements in the CKM-matrix is important in order to measure the CP-violating effect in the Standard Model. This may in turn answer one of the big cosmological questions, namely the asymmetry in the amount of matter and antimatter in the universe.

2.3 The strong interaction

As mentioned, gluons have colour charge, and therefore they couple not only to quarks, but to other gluons as well, Figure 4. The probability for emitting a gluon is proportional to α_s.

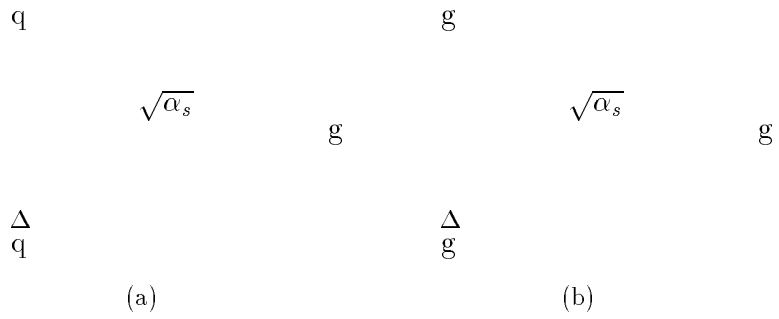

Figure 4: Feynman diagrams showing: (a) Quark emission of a gluon. (b) The gluon self-coupling.

This has important implications and is actually responsible for the fact that free quarks have never been observed, i.e. quark confinement. The strength of the strong interaction is given by the coupling constant α_s. The coupling constant can be written [2]

$$\alpha_s(Q^2) = \frac{12\pi}{(33 - 2n_f)\log(Q^2/\Lambda^2)} \tag{15}$$

where Q^2 is the four-momentum exchange of the interaction, n_f is the number of quark flavours and Λ is a scale parameter which has to be determined experimentally ($\Lambda \sim 0.2$ GeV [7]). For large momentum transfer which is associated with short-distance interactions, $\alpha_s(Q^2)$ becomes small, and therefore the interaction becomes weaker. This characteristic behaviour is

called asymptotic freedom. This is valid when $Q^2 \gg \Lambda^2$. When Q^2 is of the order of Λ^2 it is no longer true, and quarks and gluons will be bound together as hadrons. Λ marks the boundary between a small coupling constant where quarks and gluons are quasi-free, and a large coupling constant where they are bound together [2].

The picture of a baryon as three quarks bound together with gluons is way too simple. A baryon, or a meson, consists of a complicated cloud of quark-antiquark pairs, called sea-quarks, gluons and three, or two, valence-quarks. However the valence-quarks may be observed without noticing the sea-quarks [2].

2.4 Heavy Quark Effective Theory

A heavy quark Q is a quark with mass $m_Q \gg \Lambda$. This means that the c, b and t-quarks are considered heavy, whereas the other three are light quarks. In a hadron containing a heavy quark, the heavy quark is surrounded by light quark-antiquark-pairs and gluons, and the typical momenta exchanged between the heavy quark and the light constituents are of the order of Λ. The size of the hadron is given by $R_{had} \sim 1/\Lambda$, but the Compton wave length of the heavy quark $\lambda_Q \sim 1/m_Q$ is much smaller than R_{had} so the exchanged gluons with low momenta cannot resolve the heavy quark. They are only able to resolve distances much larger than λ_Q. The light constituents, which are also called the light degrees of freedom, therefore only experience the colour field of the heavy quark, and do not see the spin orientation or the flavour of it [11].

When $m_Q \to \infty$, the hadron and the heavy quark will have the same velocity, and the wave function of the light constituents will be the same as if there were a static colour source at the position of the heavy quark. That is a solution of the QCD field equations which is independent of m_Q [9]. In this limit, replacing a heavy quark with velocity v and spin s, Q(v,s), with another heavy quark with different flavour and spin, but with the same velocity v, Q$'(v, s')$, will not change the configuration of the light constituents. This means that there is a SU($2N_h$) spin-flavour symmetry group (where N_h is the number of heavy quarks) which leaves the effective strong interaction invariant [11]. This is called heavy quark effective theory (HQET), and its physical content is that in the limit $m_Q \to \infty$, the strong interactions of a heavy quark become independent of its mass and spin [10].

Together with the available four-vectors, form factors parametrize the hadronic matrix elements of the transition amplitude between two heavy quark states. The form factors are Lorentz invariant functions of q^2, which is the total four-momentum transfer in the interaction [7]. When a meson Q

with velocity v makes a weak transition into Q′ with velocity v', the hadronic element describing this transition can be expressed by one single form factor $\xi(v \cdot v')$, which is independent of m_Q. This form factor is called the Isgur-Wise function and is universal, i.e. it occurs in all matrix elements describing transitions between mesons containing a heavy quark. In the case of equal velocities the Isgur-Wise function is normalized, $\xi(1) = 1$. $v \cdot v'$ is often called ω and the limit where ω=1 (or $q^2 = q^2_{max}$) is called the zero recoil limit. The results are model-independent consequences of QCD in the limit where $m_Q \to \infty$, and can be used to determine the V_{cb}-element of the CKM-matrix [8, 9, 11].

The V_{cb}-element of the CKM-matrix is related to the probability for a b-quark decaying weakly into a c-quark, see Figure 5. With HQET, the rate for $B \to \overline{D}^* \ell^+ \nu_\ell$ when D^* is produced at rest and $\omega = 1$, is a function of $| V_{cb} |^2$ [7, 10].

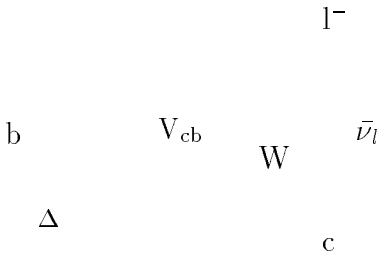

Figure 5: The probability for the weak decay of the b-quark into a c-quark is given by V_{cb}.

Corrections of order Λ/m_Q arise as the quark masses are not infinite [9]. However as long as $m_Q \gg \Lambda$ the symmetry exists. Heavy-quark symmetry is not a symmetry of the QCD-Lagrangian, but it is an approximation in a system where a heavy quark interacts by exchanging soft gluons, i.e. gluons with low momenta [11].

The total angular momentum of the light degrees of freedom is given by $\vec{j}_q = \vec{s}_q + \vec{L}$, where $\vec{s}_q$ is the spin of the light quark and $\vec{L}$ is its orbital angular momentum. HQET then implies that the spin $\vec{s}_Q$ of the heavy quark and $\vec{j}_q$ are separately conserved by the strong interaction. A state can thus be described in terms of the quantum numbers of the light constituents, since the dynamics is independent of the spin and the mass of the heavy quark.

Spin symmetry gives for the total angular momentum of the hadron

$$\vec{J} = \vec{j}_q + \vec{s}_Q = \vec{j}_q \pm \frac{1}{2} \tag{16}$$

a doublet of degenerate states for fixed $j_q \neq 0$. Flavour symmetry relates properties of states with different heavy quark flavour [10].

2.5 Orbitally excited D-mesons

D-mesons consist of a c-quark and a $\bar{u}$ or $\bar{d}$ antiquark, where both quark and antiquark have spin 1/2. For mesons with zero orbital angular momentum, i.e. ground state mesons, this gives a singlet state with total quark spin S=0 and a triplet state with S=1. The parity of a meson is given by

$$P = -(-1)^L \tag{17}$$

where L is the orbital angular momentum. The extra minus sign is due to the fact that the quark and antiquark have opposite intrinsic parity [2]. Therefore the ground state mesons yield:

$$J^P = \begin{cases} 0^- & D & pseudoscalar \\ 1^- & D^* & vector \end{cases} \tag{18}$$

The first orbitally excited states are those with orbital angular momentum L = 1, which according to the spin summation rule

$$\mathrm{J} = \mid \mathrm{L} - \mathrm{S} \mid, \mid \mathrm{L} - \mathrm{S} + 1 \mid, ..., \mathrm{L} + \mathrm{S} - 1, \mathrm{L} + \mathrm{S} \tag{19}$$

gives four states, a S=0 singlet state and a S=1 triplet state, see Table II. They can decay strongly to $\mathrm{D}^*\pi$ or $\mathrm{D}\pi$ [7], where the pion has $J^P = 0^-$ [4], and the parity of $\mathrm{D}^{(*)}\pi$ is [4]

$$\mathrm{P}_{D^{(*)}\pi} = P_{D^{(*)}} \cdot P_\pi (-1)^{L_{rel}} = (-1)^{L_{rel}} \tag{20}$$

where L_{rel} is the relative orbital angular momentum. Conservation of J^P in strong interactions gives the allowed decay modes and the relative orbital angular momentum between the decay products, see Table II.

Table II: Orbitally excited D-states, distinguished by the spectroscopic notation $^{2S+1}L_J$, and the allowed decay modes. L_{rel} is the relative angular momentum between $\mathrm{D}^{(*)}$ and π.

Orbitally excited states		Decay products	
$^{2S+1}\mathbf{L_J}$	$\mathbf{J^P}$	$D^*\pi$	$D\pi$
$^3\mathrm{P}_2$	2^+	$\mathrm{L}_{rel} = 2$	$\mathrm{L}_{rel} = 2$
$^3\mathrm{P}_1$	1^+	$\mathrm{L}_{rel} = 0, 2$	-
$^3\mathrm{P}_0$	0^+	-	$\mathrm{L}_{rel} = 0$
$^1\mathrm{P}_1$	1^+	$\mathrm{L}_{rel} = 0, 2$	-

In the approximation of HQET the mass of the c-quark is considered infinite. Since the spin $\vec{s}_Q$ of the heavy quark and the total angular momentum of the light quark $\vec{j}_q = \vec{s}_q + \vec{L}$ are separately conserved, the four states can be divided into two doublets characterized by j_q

$$j_q = \frac{1}{2} \pm 1 = \begin{cases} 1/2 \\ 3/2 \end{cases} \tag{21}$$

The total angular momentum of the heavy-light meson gives four orbitally excited states, D_J:

$$J^P = \frac{1}{2} \pm \begin{cases} 1/2 & = & \begin{cases} 0^+ & D_0^* & scalar \\ 1^+ & D_1^* & pseudovector \end{cases} \\ 3/2 & = & \begin{cases} 1^+ & D_1 & pseudovector \\ 2^+ & D_2^{*0} & tensor \end{cases} \end{cases} \tag{22}$$

It is shown in [12] that transitions to ground state mesons will follow the scheme given in Table III.

Table III: Orbitally excited D-meson states and the allowed decay modes in the heavy quark approximation.

Orbitally excited states		Decay products	
State D_J	j_q	$D^*\pi$	$D\pi$
D_2^*	$\frac{3}{2}$	$L_{rel} = 2$	$L_{rel} = 2$
D_1	$\frac{3}{2}$	$L_{rel} = 2$	-
D_1^*	$\frac{1}{2}$	$L_{rel} = 0$	-
D_0^*	$\frac{1}{2}$	-	$L_{rel} = 0$

The two states in the $j_q = 3/2$ doublet decay only through D-wave, i.e. $L_{rel} = 2$, and are therefore expected to be narrow [13], whereas the states in the $j_q = 1/2$ doublet only decay through S-wave, i.e. $L_{rel} = 0$, and should be broad. Only the narrow states can be observed experimentally.

Thus there are four neutral (with quark-antiquark combination $c\bar{u}$) and four charged ($c\bar{d}$) orbitally excited D-mesons with L = 1, which are denoted D_J or D^{**}.

3 Semileptonic decay of B-mesons to D^{**}

As mentioned, the semileptonic B-decay $\overline{B} \to D^* \ell^- \bar{\nu}_\ell$ is important because the V_{cb}-element of the CKM-matrix can be measured through this decay [7]. This requires good knowledge of the branching ratio of this decay.

About 10.1 % [7] of all B^- decay semileptonically to $\ell^- \bar{\nu}_\ell X$, where X means "anything", i.e. inclusive branching fraction. The branching ratios for b $\to$ c decays are [7]:

$B^- \to D^0 \ell^- \bar{\nu}_\ell X$	1.6 ± 0.7 %
$B^- \to D^{*0} \ell^- \bar{\nu}_\ell X$	5.3 ± 0.8 %
$B^- \to$ "D^{**0}" $\ell^- \bar{\nu}_\ell$	2.27 ± 0.7 %

The quotation marks indicate that "D^{**0}" not only includes orbitally excited D-mesons, D^0_J, but also the non-resonant decay $B^- \to D^{(*0)} \pi \ell^- \bar{\nu}_\ell$. This decay will have the same vertex topology as $B^- \to D^{**0} \ell^- \bar{\nu}_\ell$, see Figure 6.

Since D^{**} mesons decay into D^* or D, the semileptonic decay of B-mesons to D^{**} is an important background to $\overline{B} \to D^* \ell^- \bar{\nu}_\ell$. Observation of D^{**} states is also important as it will test the predictions of Heavy Quark Effective Theory.

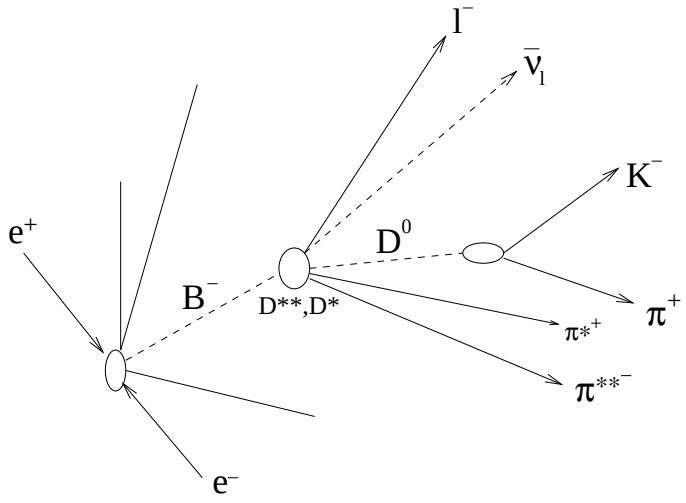

Figure 6: Vertex topology of a $B \to D^{**} \ell^- \bar{\nu}_\ell$ event. π^{**} is the pion from $D^{**} \to D^* \pi$ decay, while π^* comes from $D^* \to D^0 \pi$.

3.1 Decay modes

The existence of four neutral and four charged D^{**} states are predicted (see section 2.5) along with their properties. Not all D^{**} states are allowed to

decay both to $D^*\pi$ and $D\pi$, and the two broad D^{**} states with $j_q=\frac{1}{2}$ cannot be observed experimentally. Both neutral [17] and charged [18] D^{**} states with $j_q=\frac{3}{2}$ have been observed. Table IV gives an overview of the masses, widths and decay modes of the D^{**} states [15].

Table IV: Masses, widths and decay modes of orbitally excited D-meson states in the heavy quark approximation. The masses and widths of the narrow states are determined experimentally [7], whereas the theoretical predictions are given for the broad states [19].

Meson			Neutral States		Charged States		Decay modes
D_J	J^P	j_q	Mass (MeV/c^2)	Width (MeV/c^2)	Mass (MeV/c^2)	Width (MeV/c^2)	
D_0^*	0^+	$\frac{1}{2}$	$\sim$2360	$\gtrsim$170	$\sim$2360	$\gtrsim$170	$D\pi$
D_1^*	1^+	$\frac{1}{2}$	$\sim$2420	$\gtrsim$250	$\sim$2420	$\gtrsim$250	$D^*\pi$
D_1	1^+	$\frac{3}{2}$	2422$\pm$2	19$\pm$4	2427$\pm$5	28$\pm$8	$D^*\pi$
D_2^*	2^+	$\frac{3}{2}$	2459$\pm$2	23$\pm$5	2459$\pm$4	25$\pm$8	$D\pi$, $D^*\pi$

In the present analysis, neutral D^{**} states are studied in the following semileptonic B-decay mode[3]

$$
\begin{aligned}
B^- \longrightarrow\ & D^{**0}\,\ell^-\bar{\nu}_\ell \\
& \hookrightarrow D^+\pi^- \\
& \hookrightarrow D^{*+}\pi^- \\
& \qquad \hookrightarrow D^0\pi^+ \\
& \qquad \hookrightarrow D^+\pi^0/\gamma
\end{aligned}
$$

The study of the production of D^{**0} has been done by studying the $D^{*+} \to D^0\pi^+$ mode, where in turn the D^0 has been reconstructed in the channel $D^0 \to K^-\pi^+$. Only the narrow resonances, D_1^0 and D_2^{*0}, have been studied.

[3]Charge conjugate states are implied everywhere in the analysis. The lepton ℓ is either an electron or a muon.

3.1.1 Branching ratios

Table V shows the measured branching ratios for $B^- \to D^{**0}\ell^-\bar{\nu}_\ell$ obtained in previous analyses at LEP [20].

Table V: Branching ratios for $B^- \to D^{**0}(D^{(*)+}\pi^-)\ell^-\bar{\nu}_\ell$.

Decay	Branching Ratio (%)
$B^- \to D_J^0(D^{*+}\pi^-)l^-\bar{\nu}_l$	$2.17 \pm 0.50 \pm 0.26$ (DELPHI)
	$1.61 \pm 0.34 \pm 0.34$ (OPAL)
$B^- \to D_1^0(D^{*+}\pi^-)l^-\bar{\nu}_l$	$0.44 \pm 0.10 \pm 0.07$ (ALEPH)
$B^- \to D_2^{*0}(D^{*+}\pi^-)l^-\bar{\nu}_l$	< 0.34 (95 % c.l.) (ALEPH)
$B^- \to D_2^{*0}(D^{+}\pi^-)l^-\bar{\nu}_l$	< 0.33 (95 % c.l.) (ALEPH)
	$0.42 \pm 0.19 \pm 0.08$ (OPAL)

Table VI shows the rest of the branching ratios of interest in semileptonic B-decay into D^{**}. R_b is the ratio

$$R_b = \frac{\Gamma(Z^0 \to b\bar{b})}{\Gamma(Z^0 \to hadrons)}$$

Table VI: Branching ratios for semileptonic B-decay with $D^* \longrightarrow D^0(K\pi)\pi$ [7].

Decay	Branching Ratio (%)
R_b	22.12 ± 0.19
$b \to B^-$	37.8 ± 2.2
$D^{*+} \to D^0\pi^+$	68.3 ± 1.4
$D^0 \to K^-\pi^+$	3.83 ± 0.12

The number of D_J^0 mesons expected from a certain number of Z^0 decays in the $D^{**0} \to D^{*+}\pi^-$ channel, with $D^{*+} \to D^0\pi^+$, can now be calculated from these branching ratios:

$$\begin{aligned} N(D_J^0) = N(Z^0) \quad \times \quad & R_b \times 2 \times Br(b \to B^-) \times \\ & Br(B^- \to D_J^0(D^{*+}\pi^-)\ell^-\bar{\nu}_\ell) \times \\ & Br(D^{*+} \to D^0\pi^+) \end{aligned} \tag{23}$$

(The factor 2 is due to division of the event into two hemispheres, see section 5.4.)

The present analysis was performed on the DELPHI data from 1994 and 1995, where the 1994 data set contains 1.5 million hadronic Z^0 decays, and 1995 has 0.75 million hadronic Z^0 decays, which gives (using the most optimistic number for $B^- \to D_J^0(D^{*+}\pi^-)l^-\bar{\nu}_l$ decay):

- $\sim$5600 D^{**0} decaying to $D^{*+}(D^0\pi^+)\pi^-$.
- $\sim$210 D^{**0} with $D^0 \to K^-\pi^+$ in the final state.

3.2 Characteristics of an event

Events where a B-meson decays semileptonically to $D^{**}\ell\nu_\ell$ with the subsequent decays $D^{**} \to D^*\pi$ and $D^* \to D^0\pi$, have some characteristic properties.

3.2.1 The leptons

In semileptonic B decays a charged and a neutral lepton are produced as seen in Figure 5. Since the mass of W is large, the leptons will have large momenta. This gives an event with a large missing momentum, since the neutrino escapes detection. The charged lepton is also often emitted at large angles with respect to the direction of the B-meson, which gives a lepton with large transverse momentum [4].

3.2.2 Mass difference, ΔM

The mass difference between D^0 and D^* is small: $\Delta M_{(D^{*+}-D^0)} = 145.4$ MeV/c^2 [7]. Thus the pion coming from D^* decay is slow.

Since the mass difference between D^{**} ($M_{D^{**}} \sim 2400$ MeV/c^2, Table IV) and D^{*+} ($M_{D^{*+}} = 2010.0$ MeV/c^2) is ~ 400 MeV/c^2, and the pion mass is $M_\pi = 139.6$ MeV/c^2, the pion from D^{**} decay (called π^{**}) has high momentum compared with pions coming from fragmentation.

Instead of plotting the mass itself, the mass differences $\Delta M_{(D^{*+}-D^0)}$ for D^* and $\Delta M = (M(D^*\pi) - M(D^*))$ for D^{**} are plotted. The reason that it is more precise to plot mass differences instead of the mass itself is due to strong correlations between the errors on the masses of $D^*\pi$ and D^*. Simply speaking, if higher/lower mass on D^* is measured, then higher/lower mass of the $D^*\pi$ combination is obtained.

4 The DELPHI experiment

This chapter gives a brief introduction to CERN and the LEP collider and an overview of the DELPHI-experiment.

4.1 CERN and LEP

In 1954 the work to build the European Laboratory of Particle Physics, CERN (Conseil Européen pour la Recherche Nucléaire) began. Since 1989 has the Large Electron Positron (LEP) collider been operating. LEP has a circumference of 27 km, making it the largest particle accelerator in the world. Electrons and positrons are accelerated in opposite directions in the same beam tube due to their opposite charges. First they are accelerated in the smaller rings (the Proton Synchrotron (PS) and the Super Proton Synchrotron (SPS)) of the accelerator complex at CERN, and then injected into LEP, where they are accelerated to velocities close to the speed of light. The particles are then brought to collide in the four experimental areas where the detectors of ALEPH, OPAL, L3 and DELPHI are located.

The energy of the collider was until the end of 1995 around 91 GeV, thus making it possible to produce Z^0 (with mass 91,18 GeV/c^2) particles by collisions between electrons and positrons.

4.1.1 Z^0 decay

About 70 % of the Z^0s subsequently decay into quark-antiquark pairs. The simplest diagram for this process is showed in Figure 7. A strong interac-

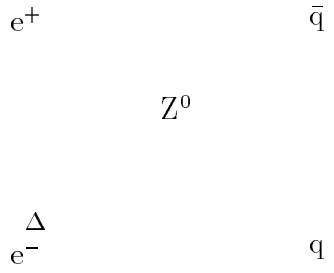

Figure 7: Feynman diagram for the annihilation of electron and positron at LEP.

tion process, called fragmentation, will then occur. It converts the quark-antiquark pair into two or more jets of hadrons which may be observed in the detector. A jet is defined by its total momentum

$$\mathbf{P} = \sum_i \mathbf{p}_i \tag{24}$$

where the sum is over all the particles in the jet [4]. The momentum transfer between the quark and antiquark in the fragmentation process is small when compared to the momentum of the quark and antiquark. Thus the direction of the jet reflects the direction of the original quark or antiquark [4]. The fragmentation process is very complicated and the contents of each jet will vary from event to event. Figure 8(a) shows a two-jet event. A gluon may also be emitted by the quark or the antiquark before the fragmentation occurs. This gives rise to three-jet events, Figure 8(b).

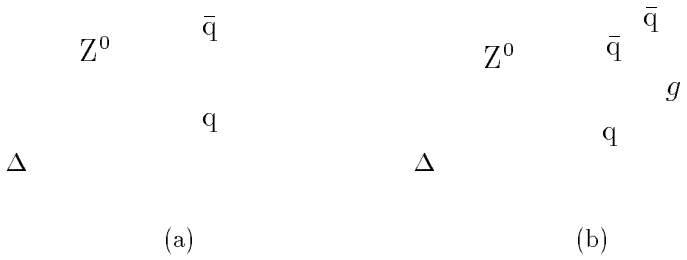

Figure 8: Feynman diagram for Z^0 decay into a: (a) two jet hadronic event and (b) three hadronic jets.

4.2 The DELPHI detector

The DELPHI (DEtector with Lepton, Photon and Hadron Identification) experiment is one of the four LEP-experiments. The detector has a cylindrical section which covers the "barrel" region which is the region with θ between 40^o and 140^o. θ is the polar angle with the z-axis where the z-axis is the direction along the electron beam. Two end-caps are mounted to cover the "forward" regions, see Figure 9.

The superconducting solenoid of DELPHI produces a uniform magnetic field of 1.2 T which is parallel to the z-axis. The magnetic field bends the trajectory of charged particles. The radius of the curvature of the track is given by [4]

$$\rho\,[m] = \frac{p\,[GeV/c]}{0.3B\,[T]} \tag{25}$$

The central part of the detector contains the tracking detectors:

- The Vertex Detector (VD)
- The Inner Detector (ID)

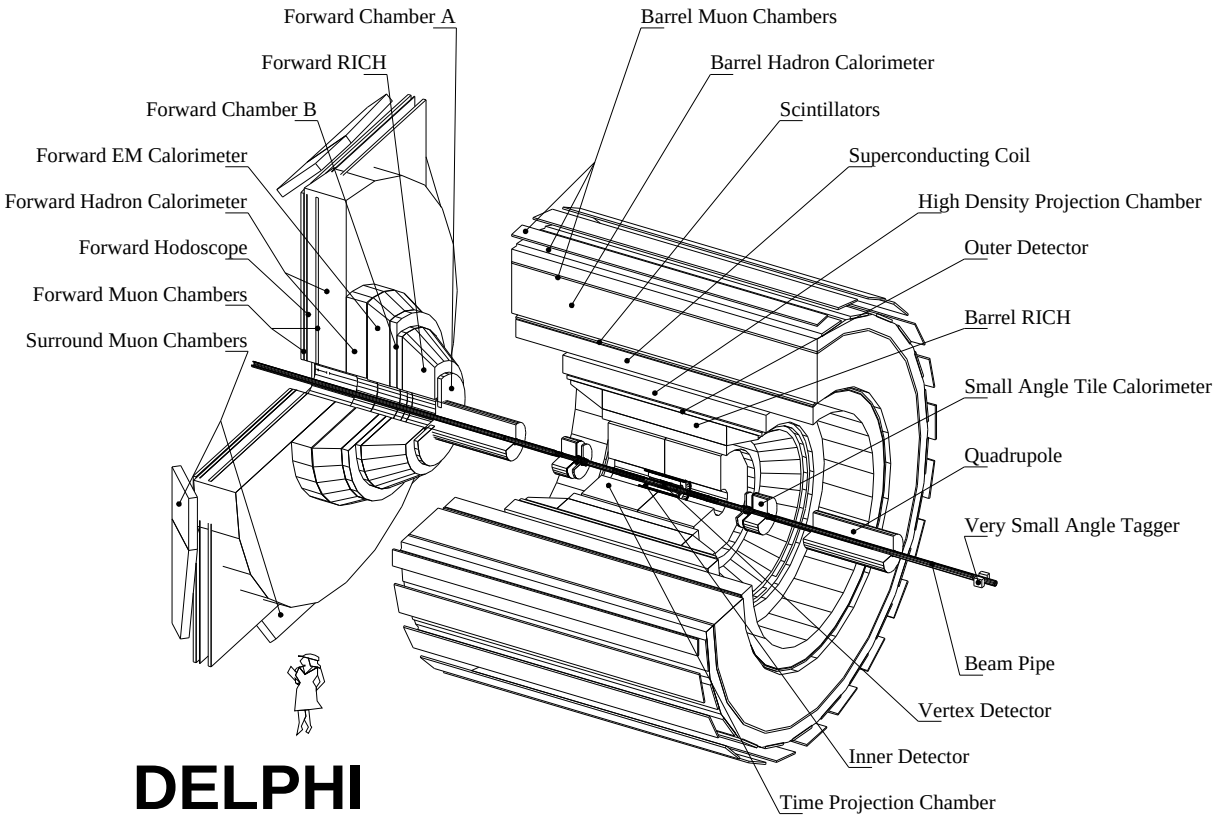

Figure 9: Overview of the DELPHI detector.

- The Time Projection Chamber (TPC)
- The Outer Detector (OD)
- The forward tracking chambers (FCA and FCB)

The detector also consists of

- Electromagnetic Calorimeters[4]
  - High density Projection Chamber (HPC)
  - Forward ElectroMagnetic Calorimeter (FEMC)
  - Small angle TIle Calorimeter (STIC) and Very Small Angle Tagger (VSAT)
- Scintillators which give a flash of light when they are hit by ionizing radiation.
- Hadron Calorimeters (HAC).
- Barrel (MUB) and Forward (MUF) muon drift chambers and the Surrounding Muon Chambers (SMC).
- Barrel and forward Ring Imaging CHerenkov (RICH) detectors.

A more detailed description can be found in [21].

4.2.1 Particle identification

Charged particles are identified in DELPHI using

- RICH detectors: the barrel and the forward RICHes.
- Energy loss per unit length (dE/dX) in the TPC.
- Electron and Muon Identification.

The basic principle behind Cherenkov detectors is that particles traversing a medium at a speed greater than the speed of light in the medium, $v_{particle} > c/n$, creates an electromagnetic shock wave. Here c is the speed of light in vacuum and n the refraction index of the medium. It turns out that the radiation is emitted at a well-defined angle, the Cherenkov angle [22]

$$cos\theta_c = c/vn = 1/n \times \sqrt{1 + m^2c^2/p^2} \tag{26}$$

The number of emitted photons can be shown to be proportional to $sin^2\theta_c$ [22].

[4]Calorimeters are detectors used for measuring the energy and position of a particle by its total absorption [4]. During the absorption the particle interacts with the calorimeter material and generates secondary particles which themselves will generate further particles, and thus a shower develops. Calorimeters can detect both charged and neutral particles. Electromagnetic calorimeters are used for detection of photons and electrons while hadronic calorimeters detect hadrons.

Ring Imaging CHerenkov detectors have two spherical surfaces centered on the interaction region or the target, where the outer surface is a mirror which focuses the radiation from the traversing particle in rings on the inner surface. The radius of the rings depends on θ_c, and therefore on the velocity of the particle [4].

The tracking detectors provide the momentum p from the curvature of the track in the magnetic field according to Equation 25. θ_c is measured from the number of detected photons and the two quantities give the mass of the particle, i.e. the identity of the particle. Parallel to this identification technique the fact that a particle with velocity lower than the speed of light in a medium does not emit Cherenkov light, is also applied (veto identification) [21].

The TPC is a gas-filled cylinder with an applied voltage which gives a uniform electric field directed along the axis. Particles traversing the gas will ionize it and the free electrons will start drifting towards the end-caps where they are detected by anode wires. The drift-times are measured and it gives the z-coordinate of the production point, since the drift velocity is given by the electric field. The anode planes have two-dimensional resolution and thus the three dimensional position of the point where the electrons are produced can be measured and the track be reconstructed [21, 22]. The charge collected at the end-caps is proportional to the energy loss of the traversing particle which provides information on the energy loss per unit length $d\mathrm{E}/d\mathrm{X}$. Since $d\mathrm{E}/d\mathrm{X}$ depends on $\beta = v/c$ it can, when the momentum of the particle is known, be used to identify the particle. Figure 10 shows how different particle hypotheses can be separated using the particle identification of the RICHes and the dE/dX measurement.

In the barrel region electrons are identified using the $d\mathrm{E}/d\mathrm{X}$ measurement of the TPC and the energy deposition in the HPC. In the end-caps they are identified by the FEMC. The probability for correct identification of electrons provides three levels of tagging corresponding to different purities: loose, standard and tight. This classifies electrons with momenta above 2 GeV/c. Typical efficiencies and misidentification probabilities are shown in Table VII

Table VII: Efficiencies and misidentification probabilities for the three electron tags.

Tag	Efficiency (%)	Misid. prob. (%)
Loose	80	$\simeq 1.6$
Standard	55	$\simeq 0.4$
Tight	45	$\simeq 0.2$

Figure 10: dE/dX and RICH information in DELPHI for a set of simulated hadronic Z decays. The figure shows the separation between different particle hypotheses.

[21]. Electron identification using a neural network has recently been developed, and this gives an improved efficiency for the "loose" and "standard" tags of $\sim$ 10 %, and for the "tight" tag of $\sim$ 38 % [23].

Muons can be separated from hadrons since most hadrons are stopped in the iron of the hadronic calorimeter, while muons with momenta above 2 GeV/c pass the hadron calorimeter and reach the Muon Chambers, where they can be detected. There are four tag levels: very loose, loose, standard and tight, see Table VIII, [21].

4.2.2 Track reconstruction

DELANA is the DELPHI Reconstruction program. It starts with the track segment seen in the TPC, and extrapolate the track outwards and inwards to the Outer and the Inner Detector to obtain candidate strings of tracks.

Table VIII: Efficiencies and misidentification probabilities for the muon tags.

Tag	Efficiency (%)	Misid. prob. (%)
Very loose	95.9 ± 0.1	5.4 ± 0.2
Loose	94.8 ± 0.1	1.5 ± 0.2
Standard	86.1 ± 0.2	0.7 ± 0.1
Tight	76.0 ± 0.2	0.4 ± 0.1

In the dead zones of the TPC, track elements from the ID and the OD are directly connected. The track elements obtained this way are passed through a track fitting processor.

Then the fitted tracks are extrapolated through the detector and Vertex Detector hits are associated to the tracks. From the calorimeters, clusters of energy are associated to charged particle tracks and from the remaining clusters neutral "tracks" are created.

Hits in the Muon Chambers are then associated to tracks for muon identification and the data from the RICHes are treated.

The resulting events are stored on Data Summary Tapes (DST) The DSTs can be accessed using the PHDST [25] Package, and afterwards SKELANA [26] can read the events and fill up standardized common blocks.

4.3 Simulations

The process $e^+e^- \rightarrow Z^0 \rightarrow q\bar{q}$ (see Figure 7) shows the production of Z^0 at LEP. However, the picture of an event is much more complex than this, and corrections to this first order diagram can be divided into three parts [24]:

- Modifications due to bremsstrahlung [22], i.e. electron emission of photons $e \rightarrow e\gamma$ or quark emission of gluons $q \rightarrow qg$.
- Higher order corrections due to loop diagrams (Figure 2) [2].
- Since quarks and gluons are confined, the fragmentation process gives jets of colourless hadrons, photons and leptons, see section 4.1.1.

Due to the complexity of each event one cannot be sure what really happened in the Z^0 decay when studying real data. A model of both the response of the complete detector and the particular physical process one wants to study is needed.

Event generators are used to generate in detail the events which could be observed by a perfect detector. Monte Carlo techniques [7] are used in

order to achieve the same average behaviour and the same fluctuations in the generated as in the real events [24]. Since detectors are not perfect, there is an additional need to simulate in detail the interaction of the particles inside the detectors.

These simulated events have to be studied to obtain information on the characteristics of the physical process one wants to study and to give an estimate of the background of the process. It allows calculation of the efficiency, i.e. how efficient one can manage to reconstruct an event. This information is then applied to the real data from the experiment.

In the DELPHI experiment it is the standard DELPHI Simulation software package, DELSIM, which generates Monte Carlo events. It consists of three components [21]:

- A model for the generation of primary physical processes [24].
- A part where a particle is followed through the DELPHI detector until it hits an active detector component.
- The particle is followed inside the active detector component and the detector response is simulated.

DELANA reconstructs events in the same format for simulated as for real data and puts them on DSTs [21].

4.4 KAL – Kinematic Analysis Language

In the present analysis KAL was used for the reconstruction of events. KAL was developed in the 1980s for use at the ARGUS experiment, and has been adapted to DELPHI by professor Gerald Eigen and Anders W. Borgland at the University of Bergen. The motivation was to provide a tool which allows less time to be spent on technical programming problems, thus giving the user the opportunity to concentrate on the physical issue.

To use KAL one has to write a KAL-script which consists of statements and this script will then be read event by event. KAL contains statements to IDENTIFY particles and to SELECT particle combinations which can be SAVEd and used in other SELECT statements. The creation of ntuples is also easy [27]. Most of the information in the DELPHI Standard Common Blocks filled by SKELANA [26] can be used. KAL is implemented in Fortran 77 [28] and "compiles" the statements in the script into a command stack, which is executed via ASSIGNED GOTO statements [27, 28].

An illustration of how KAL works is given in this example, where a reconstruction of a D^0-meson is performed in the decay channel $K^- \pi^+$:

```
kal on                                  ;Starts KAL
                                        ;Semicolon means comment

cut kasigric 1                          ;Minimum RICH tag
                                        ;necessary for Kaon identification,
                                        ;1 means loose kaon tag

cut pisigric -5                         ;Minimum RICH tag
                                        ;necessary for Pion identification,
                                        ;-5 means no identification, i.e.
                                        ;all particles tagged as pions

identify k+ k+                          ;Charged tracks are loaded into
                                        ;KAL under the kaon hypothesis
identify pi+ pi+                        ;Charged tracks loaded into
                                        ;KAL under the pion hypothesis
                                        ;This depends on the CUTs

selcc k- pi+                            ;Loop over K^-π^+
                                        ;(and K^+π^-) combinations

  save d0 dmass 0.070                   ;Save the particle combination of Kπ as
                                        ;a D^0 if the mass is within
                                        ;70 MeV of the nominal D^0 mass
endsel                                  ;End of Kπ loop


selcc d0                                ;Loop over D^0 (or its antiparticle)

  lock others                           ;Lock all tracks not used to make the D^0
    fitall                              ;in order to fit a secondary vertex only of
                                        ;the tracks contributing to D^0
    if accept = 1 then                  ;If vertex fit is OK
      dmass  = mass
      dq     = charge
      dp     = p                        ;Momentum of the D^0
      dvx    = allvxx                   ;x coordinate of the fitted vertex

      selnthd 1                         ;Select the 1st daughter of the D^0 (the Kaon)
        kp = p                          ;Kaon momentum
      endsel                            ;End loop over 1st daughter
```

```
    selnthd 2                          ;Select the 2nd daughter, i.e. the Pion
      pip = p                          ;Pion momentum
    endsel                             ;End loop over 2nd daughter

  endif

  ntupel dmass dq dp dvx kp pip @      ;Put the variables in a ntuple
  text   'D0 information' @
  tags   'dmass dq dp dvx kp pip'

unlock                                 ;Unlock tracks

endsel                                 ;End loop over D^0


return                                 ;End of KAL script
```

A complete description of KAL can be found in [27].

5 Event selection

Reconstruction of semileptonic B decays with production of orbitally excited D-mesons is done in the mode with $D^0 \to K^-\pi^+$ in the final state, i.e.:

$$
\begin{aligned}
B^- \quad \longrightarrow \quad & D^{**0}\,\ell^-\bar{\nu}_\ell \\
& \hookrightarrow D^{*+}\pi^- \\
& \qquad \hookrightarrow D^0\pi^+ \\
& \qquad\quad \hookrightarrow K^-\pi^+
\end{aligned}
$$

The vertex topology of this event with the Primary Vertex, the B decay and the D decay Vertices is shown in Figure 6.

The reconstruction procedure followed these points:

- Candidate D^0s were reconstructed from $K^-\pi^+$ combinations.
- Selection of a slow pion as the pion from $D^{*+} \to D^0\pi^+$ decay gave D^{*+} candidates.
- The D^{*+} candidates were paired with a lepton in order to select a sample of $D^{*+}\ell^-$.

  Since the mass difference $\Delta M = M(K\pi\pi) - M(K\pi)$ is small, a clear signal due to D^{*+} should be seen for this selection.
- Candidate D^{**0}s are then reconstructed by adding a pion (π^{**+}) to the $D^{*+}\ell^-$ sample.

5.1 The analysis work

The work on the present analysis started with the production of a special sample of Monte Carlo data where the B^- decays to $D^{**0}\ell^-\bar{\nu}_\ell$ with $D^0 \to K^-\pi^+$ in the final state. A Fortran routine for this selection was written, and a sample of 10 500 events was then produced by DELSIM [21] using this routine.

In order to separate between genuine D^{**} candidates and candidates which are mistaken for a D^{**}, a careful study of both the signal (genuine D^{**}) and the background (false D^{**}) is needed. The characteristics of the background and the signal are quite different for many of the available variables.

The optimal cuts reduce the background and keep the signal so as to maximize the (signal/background) ratio. By plotting the ratio (signal/background), or rather (signal/$\sqrt{\text{background}}$), the best cut values of the variables can be found.

This was soon discovered to be quite a laborious task and it has taken a lot of time to optimize the cuts. Some variables did not show differences between signal and background, while other variables did show a difference, but imposing a cut on that variable lead to substantial reduction of the signal. For the reconstruction of D^{**} reduction of the signal is crucial. As shown in section 3.1.1, even with 100 % efficiency there is only a total number of $\sim$210 events in this decay channel.

In order to check whether the cuts imposed on the variables are reasonable, the reconstruction of D^{*+} has been performed without constraining it to be a daughter of D^{**}. As already mentioned, D^{*+} is expected to show a clear signal. When a good signal had been obtained for D^{*+}, the task was to select a π^{**+} (the pion from D^{**0} decay) candidate in order to reconstruct the D^{**0}.

5.2 Simulation and data samples

A simulation set consisting of 1.8 million $Z^0 \to q\bar{q}$ events, generated as described in section 4.3, was studied. To increase the statistics on semileptonic B-decays into D^{**}, the special sample produced in this mode was used. It corresponds to about 110 million Z^0 decays (using Tables V and VI).

For real data, the entire sample of data recorded by DELPHI during the 1994 and 1995 LEP runs was used. It corresponds to 1.484 million hadronic Z^0 decays for 1994 and 0.750 million hadronic Z^0 decays for the 1995 data set [21].

5.3 Background

As shown in section 3.1 the kaon and lepton of the decay have the same charge. Selecting a combination where the kaon and the lepton have opposite signs, $K^-\ell^+$, gives the contribution to D^{*+} from $c\bar{c}$ events, as can be seen from comparison of Figures 11 and 12.

In the reconstruction of D^{**}, candidate D^*s are paired with candidate π^{**}s. The background is due to semileptonic decay of the B-meson into D^* which is then combined with a fake π^{**}, i.e. a pion stemming from the fragmentation of the quarks and wrongly taken for the π^{**}. Correct sign $D^*\ell$ combination, but wrong sign on the π^{**}, gives the background for selecting the wrong π^{**} associated with D^*.

Background events without any D^{**} production have been studied on the same Monte Carlo sample as signal events.

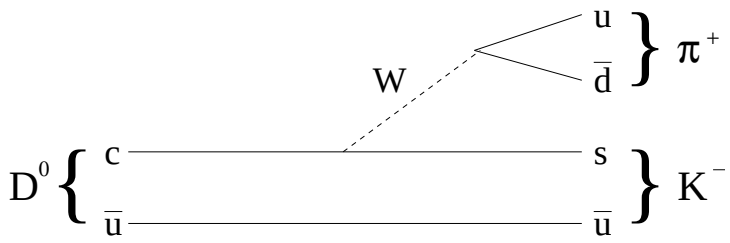

Figure 11: The dominating diagram for the decay of D^0-meson to $K^-\pi^+$ in semileptonic B-decay.

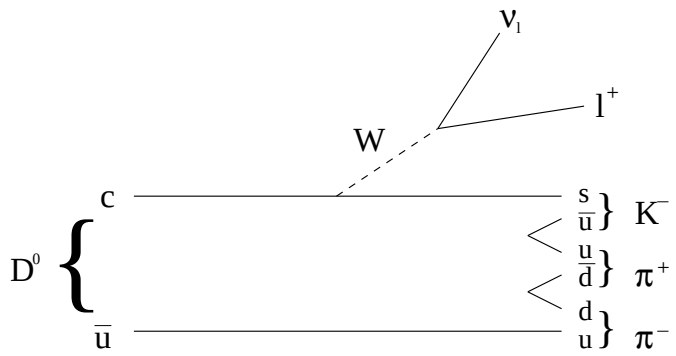

Figure 12: In the case of a $c\bar{c}$ event, the D-meson decays semileptonically, giving wrong sign combinations of kaon and lepton compared to semileptonic decay of a B-meson.

5.4 Cuts imposed on all tracks

For every event neutral and charged particles are combined and passed through a jet-finding algorithm using LUCLUS [24], which is contained in the JETSET library [24]. This jet algorithm provides the four vector of each jet in the event.

Two hemispheres are defined by a plane perpendicular to the thrust axis which is computed using all charged and neutral tracks. If the angle between a particle and the thrust axis is less than 90°, it is assigned to hemisphere 1, otherwise to hemisphere 2. The thrust is defined by [24]

$$T = \max_{|\mathbf{n}|=1} \frac{\sum_i | \mathbf{n} \cdot \mathbf{p_i} |}{\sum_i | \mathbf{p_i} |} \tag{27}$$

and the thrust axis is given by the $\mathbf{n}$ vector for which the maximum is reached.

Some cuts imposed on charged tracks are initialized in the Standard Common Blocks filled with SKELANA [26]. They are traditional cuts used by DELPHI in order to choose good hadronic events (the so-called "Team 4" selections) [26]:

- Track momentum > 0.4 GeV/c
- Relative error ΔE/E < 100 %
- Track length > 30.0 cm.
- Impact parameter[5] R/Phi < 4.0 cm.
- Impact parameter Z < 10.0 cm.
- Polar angle θ > 20.0 °

The efficiency for selecting hadronic Z^0 decays is over 95 % and the background which is mainly from $\tau^+\tau^-$ pairs and $\gamma\gamma$ collisions, is below 0.7 % [21].

5.5 $D^{*+}\ell^-$ selection

This section gives an overview of the selection criteria that has been applied in order to select a $D^{*+}\ell^-$ sample. The D^{*+} candidates are reconstructed in the $D^{*+} \to D^0\pi^+$ channel and the D^0 candidates in the $D^0 \to K^-\pi^+$ channel.

Since all particles in the decay chain originate from the decay of the same B-meson, only kaons and pions in the same jet as the lepton candidate were considered.

5.5.1 D^0 reconstruction

First a D^0 decay vertex was fitted [27, 29] in three dimensions using one kaon and one pion track. The vertex was required to have a χ^2 (see Appendix A.4) probability of at least 0.5% to suppress contributions from random tracks and badly reconstructed vertices. Figure 13 shows the χ^2-probability for both signal and background and from studies of (signal/$\sqrt{\text{background}}$) it is found that requiring a χ^2-probability above 0.5 % gives the best ratio of signal to background.

[5]The impact parameter is defined as the distance from the reconstructed vertex (in this case the primary) to the point of closest approach of a charged particle, and its sign is defined with respect to the direction of the jet [21].

The charge of the kaon had to have the same sign as the lepton charge and both the kaon and the pion had to have at least one hit in the Vertex Detector in order to reject poorly determined tracks.

The momenta of the kaon and the pion were required to be larger than 1 GeV/c, and the momentum was recalculated after imposing that the track actually came from the D^0 decay vertex.

The angle θ^* between the D^0 flight direction and the kaon direction in the D^0 rest frame had to satisfy the requirement $\cos\theta^* > -0.9$. While the background is peaked in the backward direction, the signal distribution is more isotropic because D^0, K^- and π^+ are pseudoscalar mesons. Figure 14 shows the distribution of $\cos\theta^*$ for Monte Carlo simulated data both for signal and background events.

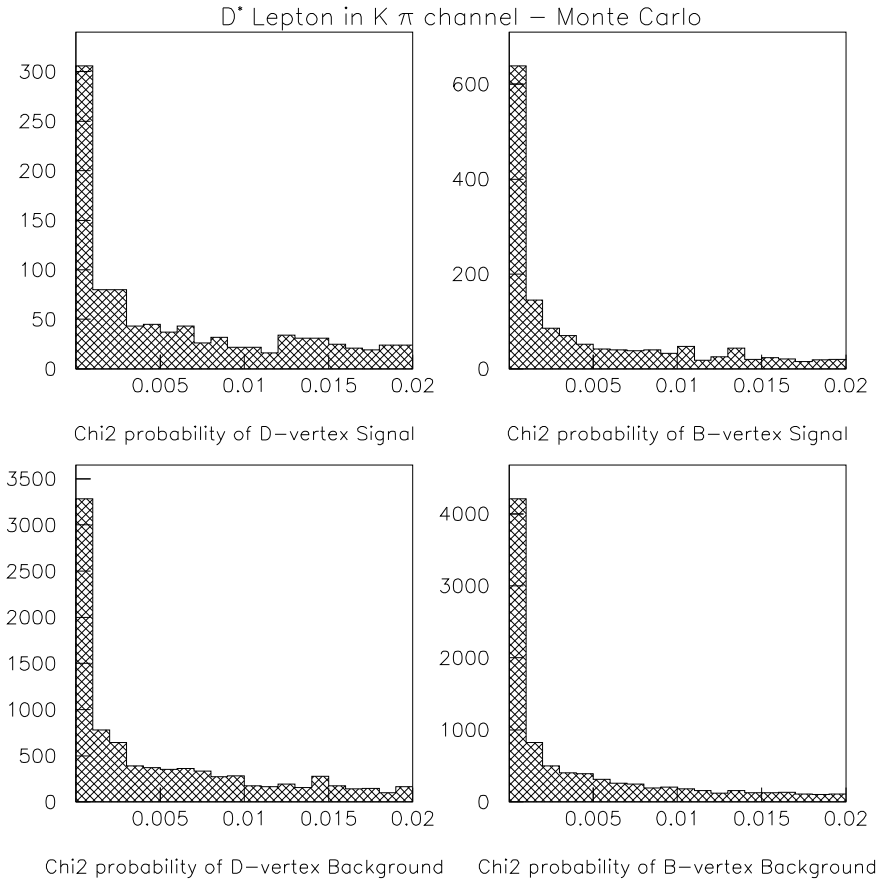

Figure 13: χ^2-probability for the D-decay vertex and the B-decay vertex for signal (top) and background (bottom).

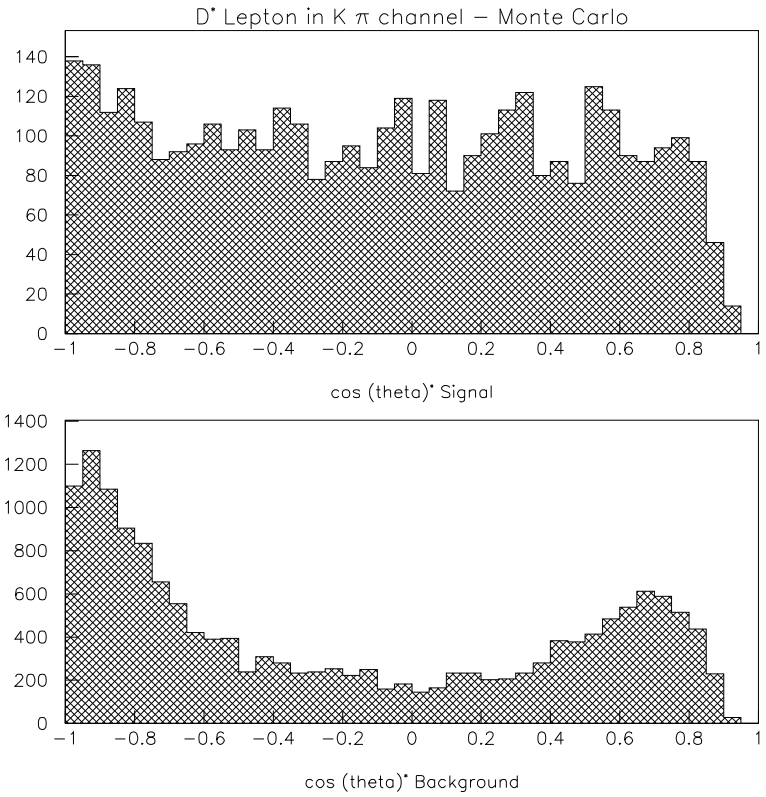

Figure 14: $\cos\theta^*$ for signal (top) and background (bottom).

For the reconstruction of D^{*+} the mass of the $K^-\pi^+$ combination was required to be within ± 70 MeV/c^2 of the nominal D^0 mass. A mass constrained fit was performed on the $K^-\pi^+$ combination, i.e. the energy and momentum of the particle was adjusted with the following constraint: $M_{D^0} = \sqrt{E^2 - p^2} = M_{D^0}(\text{particle table})$.

5.5.2 Lepton selection

The lepton momentum had to be greater than 2.0 GeV/c and the transverse momentum of the lepton with respect to the jet axis was required to exceed 0.4 GeV/c. The transverse momentum of a particle with respect to the jet, P_T^{jet}, is computed after removing the particle from the jet and then recomputing the jet direction.

The lepton was also required to have at least one hit in the Vertex Detector.

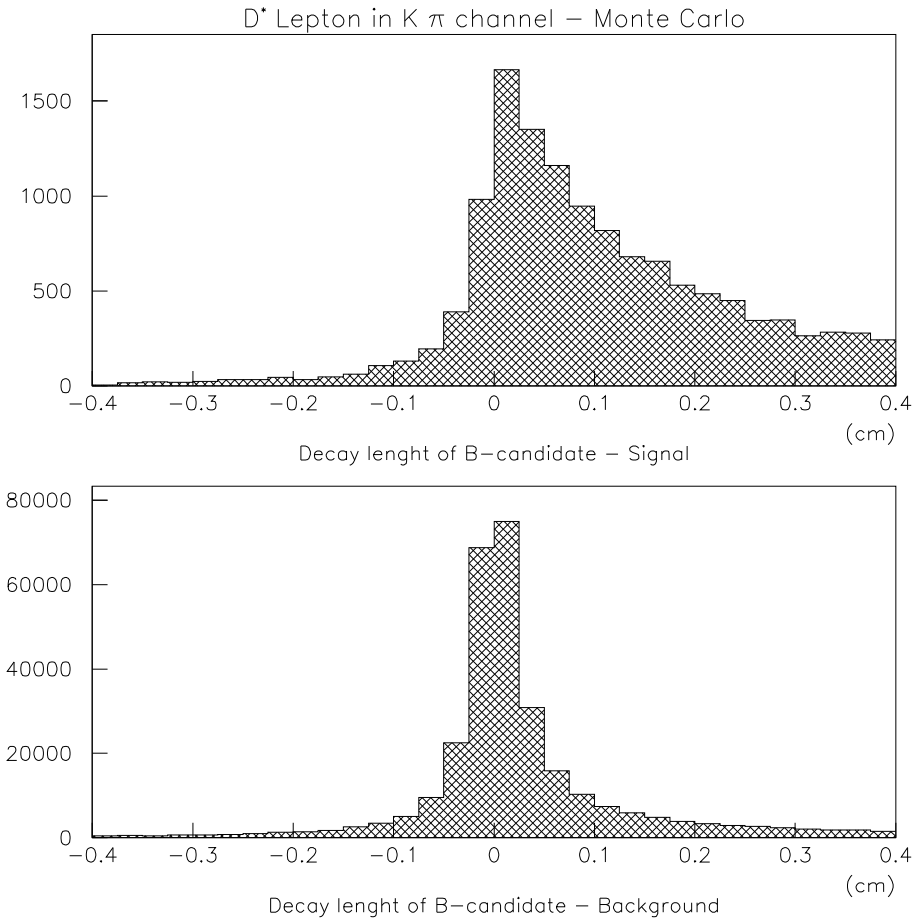

Figure 15: The distribution of the B decay length for signal and background.

5.5.3 $D^{*+}\ell^-$ vertex

A pion with the opposite charge of the lepton and the kaon was selected as the pion from D^{*+} decay (π^*). Then a $D^0\pi^+\ell^-$ vertex was fitted and the χ^2 probability of this B decay vertex was required to be greater than 0.5% (Figure 13).

Figure 15 shows the distribution of the B decay length defined as

$$B_{DL} = \{(x_{BV} - x_{PV}) \times p_x + (y_{BV} - y_{PV}) \times p_y + (z_{BV} - z_{PV}) \times p_z\}/|\vec{p}| \quad (28)$$

for Monte Carlo signal and background. Here x_{BV} and x_{PV} denotes the x-coordinate of the B-decay Vertex and the Primary Vertex respectively, p_x is the momentum of the B-meson i the x-direction, etc.. In the case of background events a larger fraction of the distribution has B_{DL} less than

zero. For the signal, B_{DL} is more likely to be positive, and the decay length of the B-meson was required to exceed 400 μm since this gave the best (signal/$\sqrt{\text{background}}$) ratio.

As mentioned earlier, the π^* is slow. Figure 16 shows the distribution of the pion momentum for the Monte Carlo *generator* particles[6]. The momentum was recalculated after imposing that the π^* originated from the B-vertex and it was required to be in the range 0.4 to 3.0 GeV/c.

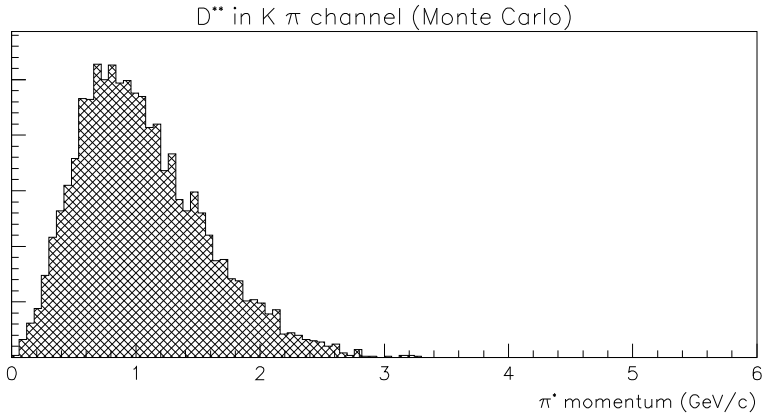

Figure 16: The momentum distribution of the π^* for Monte Carlo generator particles.

The fraction of the energy of D^* with respect to the beam energy $X_E = E(D^*)/E_{beam}$ was chosen to be between 0.15 and 1. The signal tends to have higher values of X_E than the background, see Figure 17.

[6] Monte Carlo generated particles contain all the information from the event generator, which means the Monte Carlo truth. In this case it shows how the π^* momentum truly is distributed.

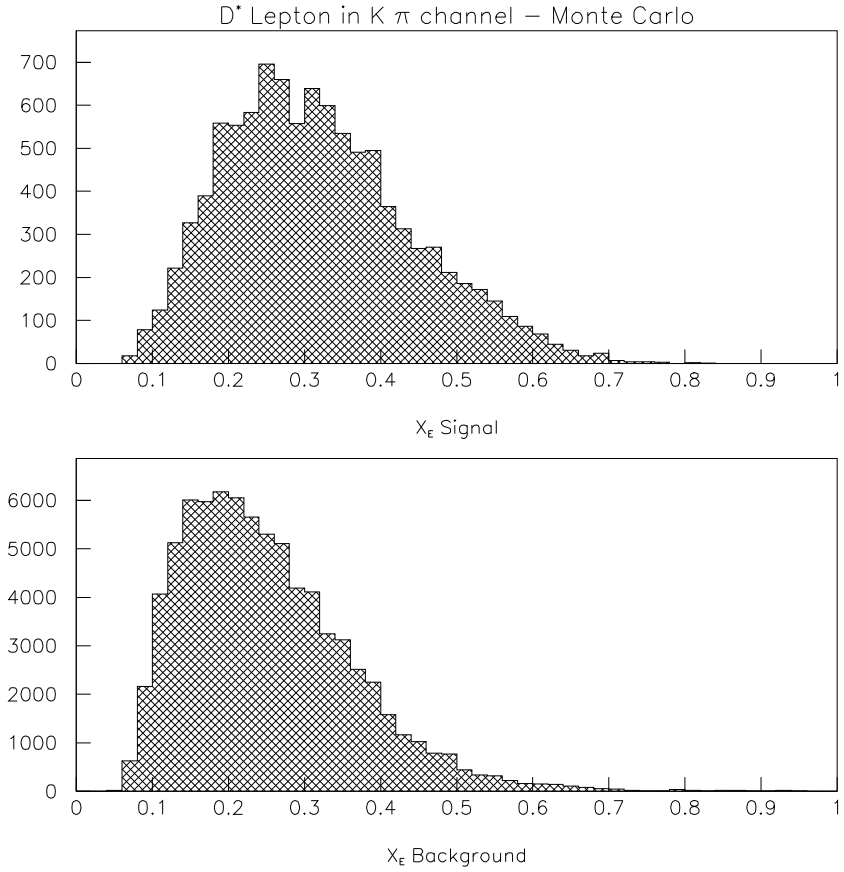

Figure 17: $X_E = E(D^*)/E_{beam}$ for signal and background.

After each cut a Gaussian function (Appendix A.1) was fitted to the D^{*+} signal of the Monte Carlo data. The mean and variance of the distribution were left as free parameters in the fit together with the number of events in the peak. An overview of the number of fitted D^*s and the reconstruction efficiencies for the cuts applied in the selection is given in Table IX. After all the cuts one finds that the total reconstruction efficiency for D^* is (19.0 $\pm$ 0.4)%.

A linear function was used for the fit of the background, and the method of maximum likelihood (Appendix A.3) was applied to fit the parameters.

Table IX: Number of reconstructed D^*s and cumulative reconstruction efficiencies for various cuts. The sample consisted of 11914 Monte Carlo generated D^*s produced in semileptonic B decays.

Cut	# of reconstructed D^*s	Cum. Eff. (%)
$P_{kaon} > 1.0\,GeV/c$ $0.4\,GeV/c < P_{\pi^*} < 3.0\,GeV/c$ $P_{lepton} > 2.0\,GeV/c$	6422 $\pm$ 82	53.9 $\pm$ 0.7
$P_{T,lepton}^{jet} > 0.4\,GeV/c$	5289 $\pm$ 74	44.4 $\pm$ 0.6
K,π,π^*,ℓ in same jet	4304 $\pm$ 67	36.1 $\pm$ 0.5
$P_{\pi} > 1.0\,GeV/c$	4110 $\pm$ 65	34.5 $\pm$ 0.5
B decay length > 400 μm	3391 $\pm$ 59	28.5 $\pm$ 0.5
# VD-hits for K,π,$\ell \geq 1$	3141 $\pm$ 54	26.4 $\pm$ 0.4
$0.15 < X_E < 1.0$	3045 $\pm$ 56	25.6 $\pm$ 0.5
χ^2 prob. D-decay vertex > 0.5 %	2767 $\pm$ 53	23.2 $\pm$ 0.4
χ^2 prob. B-decay vertex > 0.5 %	2351 $\pm$ 49	19.7 $\pm$ 0.4
$\cos\theta^* > -0.9$	2261 $\pm$ 48	19.0 $\pm$ 0.4
M_{D^0} within $\pm$ 70 MeV/c^2 of nominal value	2261 $\pm$ 48	19.0 $\pm$ 0.4

5.5.4 Identification of particles

Electrons were tagged as "very loose" [26], while muons were tagged as "loose" [21]. No identification for kaons or pions were required.

Table X shows how the reconstruction efficiency changes when tighter cuts for the particle identification are applied. The kaon identification refers to the "combined" tag, i.e. hadron identification based on combined RICH and TPC probabilities [26].

Table X: The impact of particle identification on the reconstruction efficiency for D^*.

Electron ID	Muon ID	Rec. efficiency (%)
Very Loose	Loose	19.3 ± 0.4
Loose	Loose	12.1 ± 0.3
Loose	Standard	11.2 ± 0.3
Standard	Standard	10.6 ± 0.3

Kaon Identification	
None	19.3 ± 0.4
Loose	11.9 ± 0.3
Standard	9.5 ± 0.3

5.6 $D^{**0} \to D^{*+}\pi^-$ selection

In order to reconstruct the D^{**0}, where D^{**0} for the present means the two narrow states, namely D_1^0 and D_2^{*0}, the criteria of the $D^{*+}\ell^-$ selection were applied. A $D^{*+}\ell^-\pi^{**-}$ vertex was fitted in space, and in addition to require a χ^2-probability greater than 0.5% for both this vertex (the B-decay vertex) and the D-decay vertex, both vertices were also required to be "downstream". "Downstream" means that the cosine of the angle between the momentum vector of all the tracks coming from the B-meson and the vector $(\vec{x}_{SV} - \vec{x}_{PV})$ (where $\vec{x}_{SV}$ is the coordinates of the secondary vertex and $\vec{x}_{PV}$ those of the primary), is positive. This is illustrated in Figure 18.

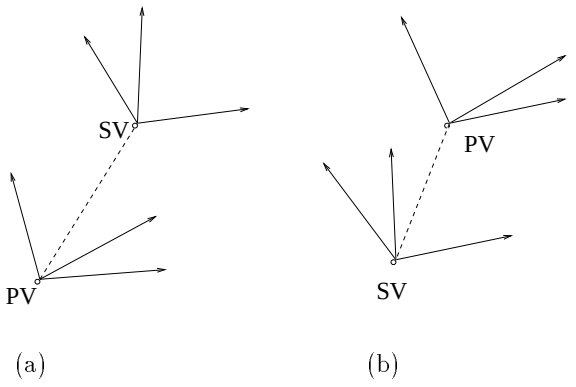

Figure 18: (a) shows an event where the secondary vertex (SV) is downstream, whereas in (b) it is not downstream.

For the present selection the mass of the $K^-\pi^+$ combination was required to be within $\pm$ 60 MeV/c^2 of the nominal D^0 mass. The mass difference $\Delta M = M(K\pi\pi) - M(K\pi)$ had to be within two standard deviations of the central value obtained from the Gaussian fit to the $\Delta M = M(K\pi\pi) - M(K\pi)$ distribution obtained from real data, see Figure 22. The fit gives 2σ = 1.5 MeV/c^2.

5.6.1 π^{**} selection

The π^{**} has, as illustrated in Figure 19(top), high momentum compared with pions from fragmentation, Figure 19(bottom). Pions with momentum higher than 1.2 GeV/c and charge of the opposite sign of the D^* charge were selected as π^{**} candidates.

In order to get rid of kaons taken for π^{**} candidates, which will give a contribution of too high ΔM, it was needed to use some particle identification for π^{**}. Only candidates with a "loose" pion tag according to the combined RICH and TPC identification [21, 26] were considered.

The selection efficiencies both for D^{*+}, D_1^0 and D_2^{*0} obtained when these cuts were applied are shown in Table XI. They are obtained after a Gaussian fit for D^{*+} (section 5.5) and the fit described below for D_1^0 and D_2^{*0}.

Table XI: Reconstruction efficiency of D^*, D_1^0 and D_2^{*0}. The sample consisted of $B \to D_J^0 \ell \bar{\nu}_\ell$ decays, with 3701 Monte Carlo generated D_1^0s, 1367 D_2^{*0}s and 5083 D^*s coming from $D_J^0 \to D^{*+}\pi^-$ decay.

Cut	Rec. eff. D^* (%)	Rec. eff. D_1^0 (%)	Rec. eff. D_2^{*0} (%)
D^* selection	21.0 $\pm$ 0.7	17.9 $\pm$ 1.1	14.7 $\pm$ 1.2
Vertices downstream	20.9 $\pm$ 0.6	17.9 $\pm$ 1.1	14.5 $\pm$ 1.2
$P_{\pi^{**}} > 1.2$ GeV/c	15.1 $\pm$ 0.5	13.9 $\pm$ 0.7	11.2 $\pm$ 1.0
Loose pion ID	11.5 $\pm$ 0.5	11.4 $\pm$ 0.9	8.9 $\pm$ 0.9

This gives an overall reconstruction efficiency of (10.4 $\pm$ 0.9)% for D_J^0 and (11.5 $\pm$ 0.5)% for D^{*+}.

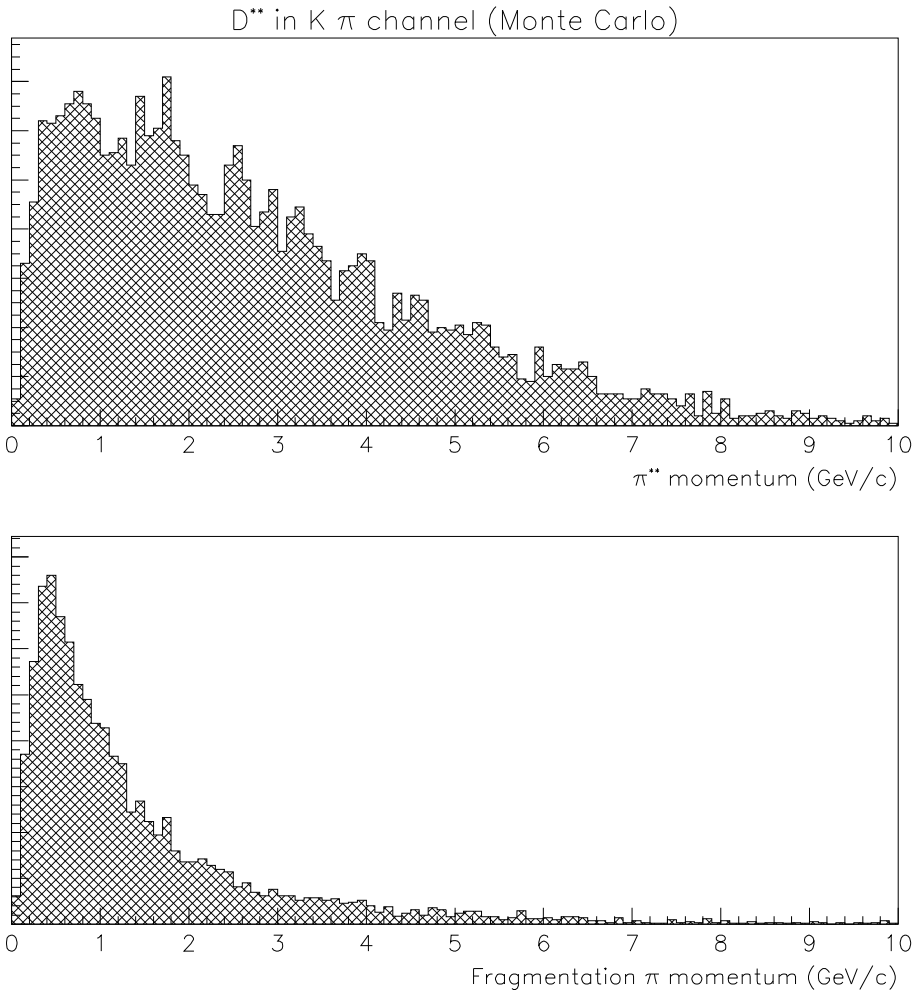

Figure 19: The momentum distribution of π^{**}(top) and pions from fragmentation(bottom), both distributions are for Monte Carlo generator particles.

5.6.2 Fits to ΔM

Figure 20 shows the mass difference $\Delta M = M(D^*\pi) - M(D^*)$ which are obtained from the Monte Carlo sample after applying the previously mentioned cuts. Breit-Wigner functions (see Appendix A.2) have been fitted to these distributions. The two distributions on top of Figure 20 shows ΔM of D_1^0 and D_2^{*0} respectively. The Breit-Wigner fits to these distributions allowed the central value and width together with the number of events in the peak, to vary. The results for the central value and width are shown in Table XII.

The difference in central value of D_1^0 and D_2^{*0} is 40 MeV/c^2.

Table XII: Central value and width of $\Delta M = M(D^*\pi) - M(D^*)$ for the two narrow D_J^0 states as obtained from Monte Carlo data.

D_J^0	Central Value (MeV/c^2)	Width (MeV/c^2)
D_1^0	410.9 ± 0.6	17.3 ± 3.0
D_2^{*0}	451.3 ± 1.9	29.6 ± 5.8

Figure 20 also shows the distribution of both D^{**} states when one does not try to separate them. In this case two Breit-Wigner functions are fitted to the distribution. The central value of the state with lowest ΔM (D_1^0) and the number of events in the peaks are free parameters in the fit. The widths of the states are fixed at the value obtained from the previous fits, and the difference in central value of 40 MeV/c^2 is given as a constant in the fit.

In all the fits a function of the form $(\alpha\sqrt{\Delta M - M_\pi}\exp[-\beta(\Delta M - M_\pi)])$ is used to describe the background (although the background is close to zero in these plots). Figure 21 shows the background where a fit using this function has been applied. α and β are free parameters in the fit.

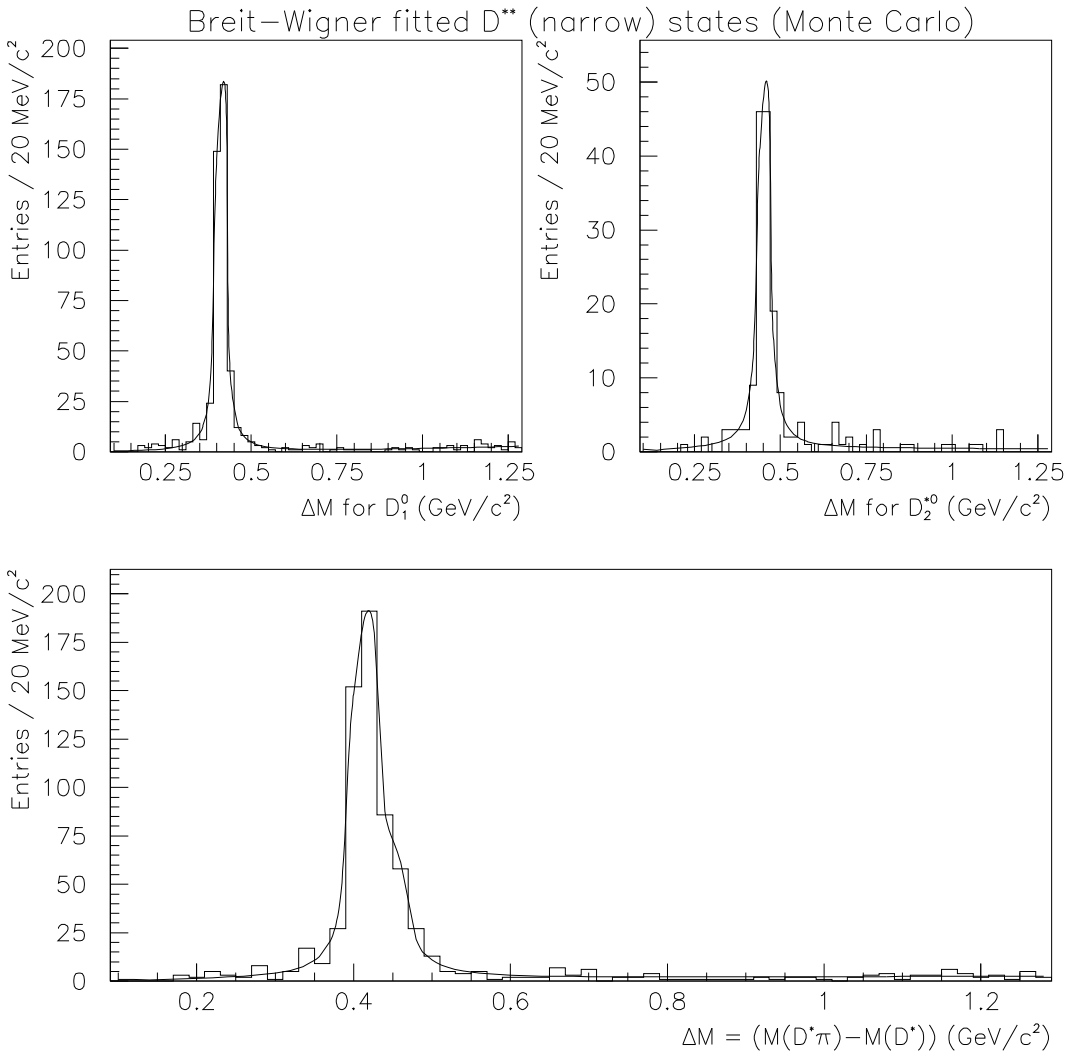

Figure 20: Mass differences for D_1^0 and D_2^{*0} (top) and both states plotted together (bottom).

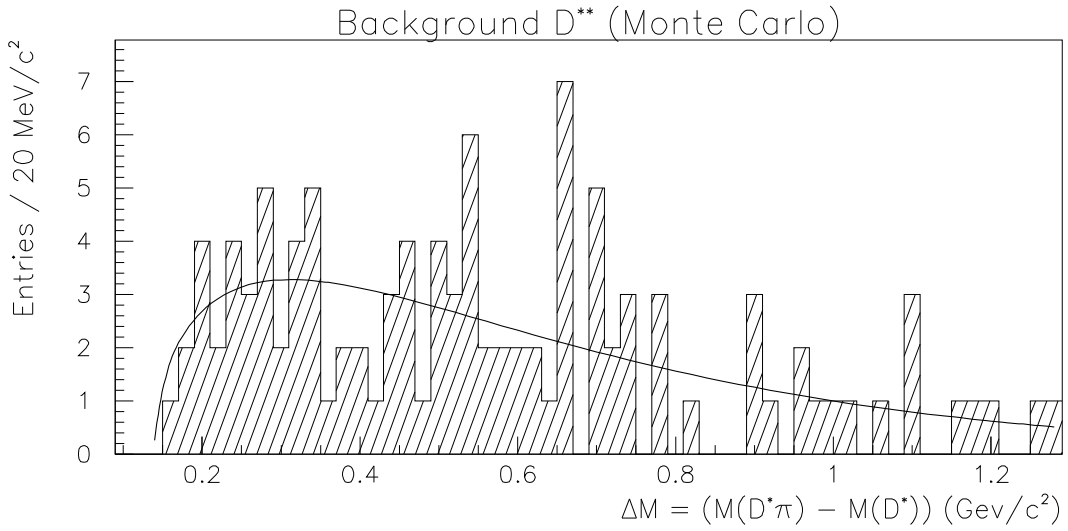

Figure 21: The figure shows the fit to the D** background distribution using the function $(\alpha\sqrt{\Delta M - M_\pi}\exp[-\beta(\Delta M - M_\pi)])$.

6 Results of the 1994 - 95 data

The following sections show the results obtained after an analysis of the full sample of DELPHI data from the 1994 and 1995 LEP runs.

6.1 D^* results

The distribution of $\Delta M = M(K\pi\pi) - M(K\pi)$ is shown in Figure 22.

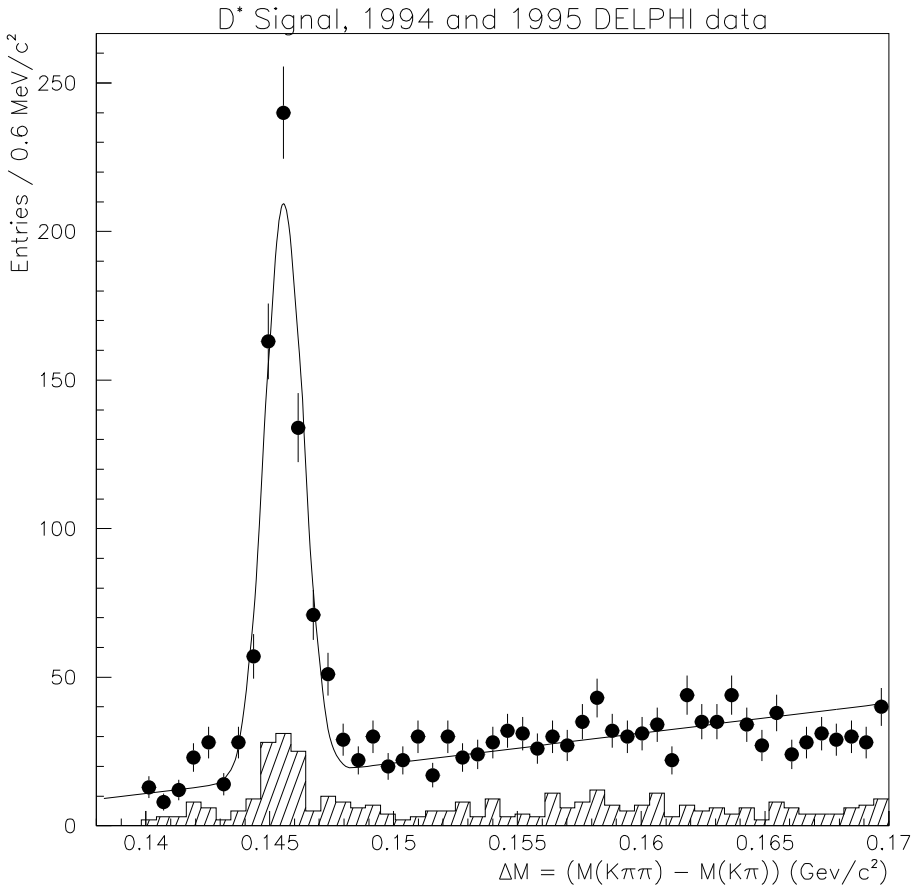

Figure 22: The mass difference $\Delta M = M(K\pi\pi) - M(K\pi)$ for the 94 and 95 data. The hatched histogram shows the contribution from the wrong sign $K^-\ell^+$ combination.

A Gaussian fit was applied to the signal with a linear function to fit the background (section 5.5). The number of fitted D^*s is (619 $\pm$ 29). The central value of the peak is (145.56 $\pm$ 0.04) MeV/c^2 which is slightly

higher than the table value of (145.42 $\pm$ 0.05) MeV/c^2 [7], and the standard deviation of the Gaussian is σ = (0.76 $\pm$ 0.04) MeV/c^2.

The hatched histogram shows the contribution from the wrong sign $K^-\ell^+$ combination due to $c\bar{c}$ events. A Gaussian fit to the wrong sign distribution gave a contribution of (83 $\pm$ 11) D^*s, Figure 23.

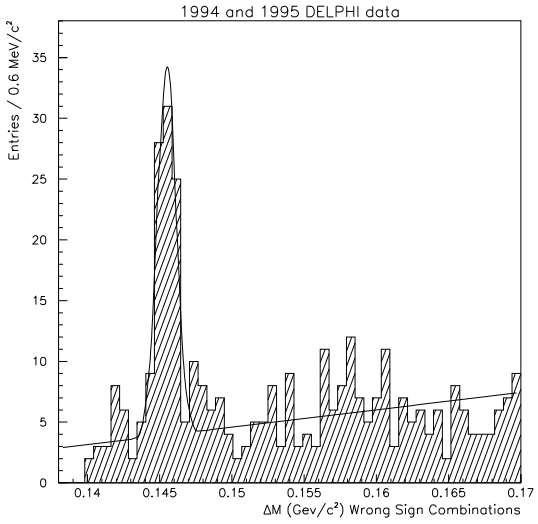

Figure 23: The mass difference $\Delta M = M(K\pi\pi) - M(K\pi)$ for the wrong sign $K^-\ell^+$ combination due to $c\bar{c}$ events.

Indeed the applied selection criteria give a clear signal for D^*.

6.2 Results of the D^{**} selection

Figure 24 shows the result after the applied selection. The dotted and the hatched histograms represent the wrong-sign lepton background ($K^-\ell^+$ combinations) and the wrong-sign pion ($D^{*+}\pi^{**+}$) background respectively. Two Breit-Wigner functions were fitted to the distribution as described in section 5.6.2.

The total number of fitted events is (16.2 $\pm$ 8.8) and the central value of the first peak is (406.3 $\pm$ 4.3) MeV/c^2 in agreement with the result obtained for Monte Carlo data shown in Table XII.

The branching ratio for the decay $B^- \to D^0_J(D^{*+}\pi^-)\ell^-\bar{\nu}_\ell$ can then be calculated according to Equation 23 with the use of Table VI. The calculation gives

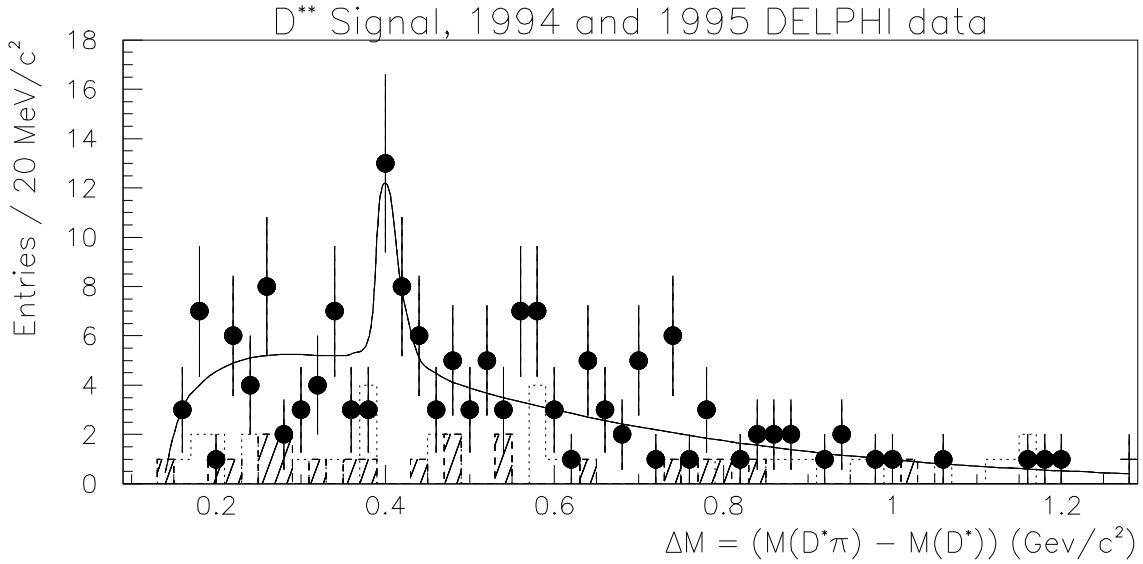

Figure 24: The signal of D^{**} in the $\Delta M = M(D^*\pi) - M(D^*)$ distribution.

$$Br(B^- \to D^0_J(D^{*+}\pi^-)\ell^-\bar{\nu}_\ell) = \frac{N(D^0_J)/\epsilon_D}{N(Z^0) \times R_b \times 2 \times Br(b \to B^-) \times Br(D^{*+} \to D^0\pi^+) \times Br(D^0 \to K^-\pi^+)} = \underline{(1.6 \pm 0.9)\,\%} \quad (29)$$

The efficiency $\epsilon_D = 10.4\%$ is included, and D^0_J stands for the two narrow states, D^0_1 and D^{*0}_2.

This measurement of the branching ratio agrees with previous results shown in Table V.

Figure 25 shows the signal of D^* in the $\Delta M = M(K\pi\pi) - M(K\pi)$ distribution after the D^{**} selection has been applied. A Gaussian fit to this distribution gives (169 ± 13) fitted events with a central value of (145.49 ± 0.05) MeV/c^2. This value is in better agreement with the nominal value of ΔM [7] than the value obtained in section 6.1. This is probably due to the harder cuts applied in the D^{**} selection.

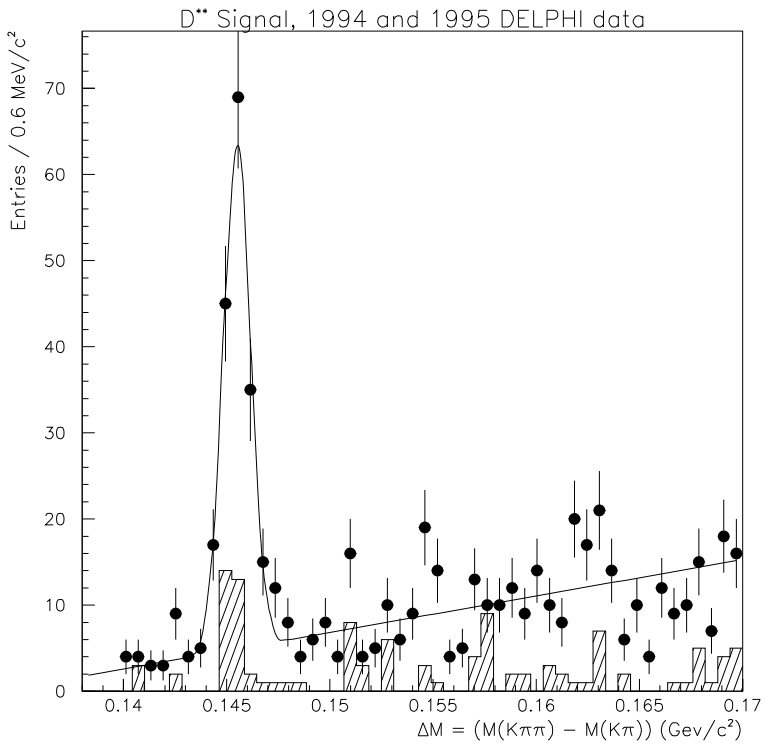

Figure 25: $\Delta M = M(K\pi\pi) - M(K\pi)$ as it has been reconstructed after applying the constraints of the D^{**} selection.

7 Discussion of the results

The background is obviously still a problem in Figure 24. In Figure 26 the background (hatched histogram) that one obtains from Monte Carlo data (Figure 21) is superimposed on the D** signal. It is observed that most of the background can be accounted for using the Monte Carlo data.

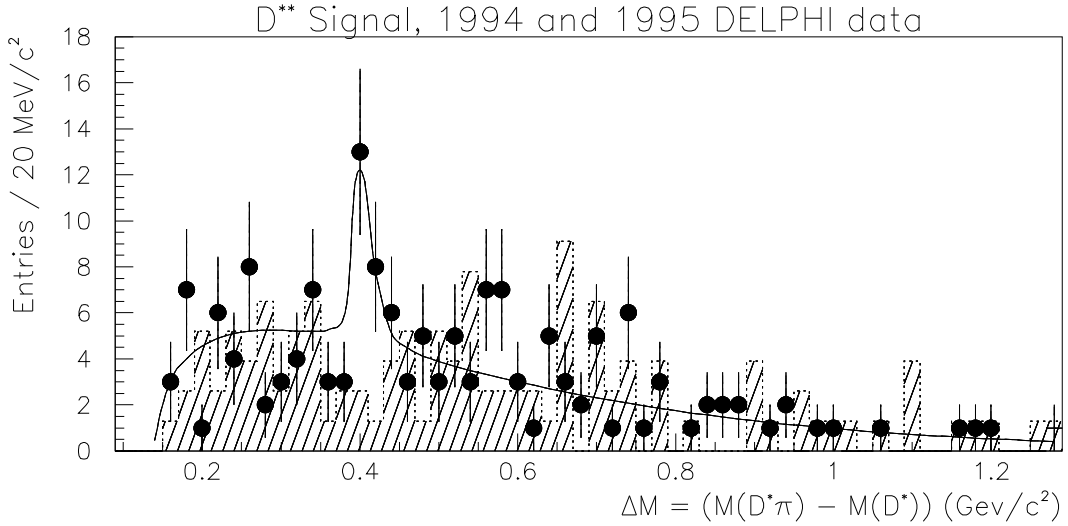

Figure 26: The distributions shows $\Delta M = M(D^*\pi) - M(D^*)$ of the signal with an overlap of the background obtained from Monte Carlo studies.

Previous analyses [14, 15, 16] have used as a selection criteria the fact that the π^{**} originates at the B decay vertex, consequently the impact parameter of the track with respect to this vertex should be small. Correspondingly the impact parameter of the π^{**} track with respect to the primary vertex should be large. For instance may the ratio

$$R_z = \frac{IP_z(\text{B}-\text{decay Vertex})\sigma_{IP}(\text{Primary Vertex})}{\sigma_{IP}(\text{B}-\text{decay Vertex})IP_z(\text{Primary Vertex})} \tag{30}$$

be calculated [14]. IP_z is the impact parameter in the z direction with respect to the B-decay vertex or the primary vertex, and σ_{IP} is the corresponding error on the impact parameter (accounting both for the error on the vertex and on the track itself). Figure 27 shows the distribution of R_z for Monte Carlo data both for π^{**} and for pions coming from fragmentation. In the present analysis this variable was studied using Monte Carlo data, and it was found that too much of the signal was lost compared with the background,

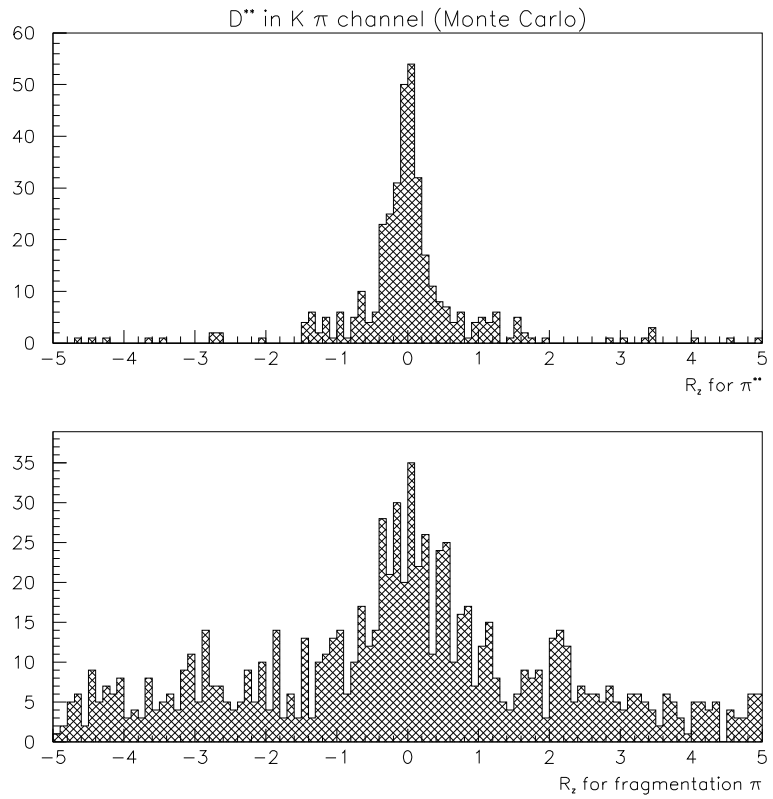

Figure 27: The ratio R_z for π^{**} and for pions coming from fragmentation.

i.e. the (signal/background) ratio was not optimized. It was therefore not applied as a selection criteria.

In the present analysis it seems that the cut at 1.2 GeV/c for the pion momentum together with the "loose" pion identification give good separation between genuine π^{**}s and pions from fragmentation even without a cut on impact parameters.

7.1 Upper limit on $Br(\mathrm{B}^- \to \mathrm{D}^0_\mathrm{J}(\mathrm{D}^{*+}\pi^-)\ell^-\bar{\nu}_\ell)$

The branching ratio $Br(\mathrm{B}^- \to \mathrm{D}^0_\mathrm{J}(\mathrm{D}^{*+}\pi^-)\ell^-\bar{\nu}_\ell) = (\,1.6 \pm 0.9\,)\,\%$ is within 2σ from zero. A preliminary upper limit on the branching ratio can be estimated using some simple approximations. Assuming the number of signal events to be distributed as a Gaussian, the 95 % confidence level can be found according to [30]

$$\mathrm{N} = n + 1.64 \cdot \sigma_n \tag{31}$$

where σ_n is the uncertainty in the number of events obtained in the fit to the ΔM distribution. If n events are found, then the probability that the true value is less than N is 95 %. The estimates obtained from the fit are:

$$n = 16.2,\ \sigma_n = 8.8$$

which gives the upper limit for the branching ratio

$$Br(\mathrm{B}^- \to \mathrm{D}^0_\mathrm{J}(\mathrm{D}^{*+}\pi^-)\ell^-\bar{\nu}_\ell) < \underline{3.0\,\%,\ (95\%\ \mathrm{C.L.})}$$

7.2 Comments

Not all parts of the detector are working perfectly during the runs. The efficiency for D^0_J reconstruction was obtained from Monte Carlo assuming all parts of the detector operating with 100 % efficiency. Since this is not the case for real events, the estimate of the reconstruction efficiency is too high.

To compensate for this, run quality cuts can be applied to the events in order to only select events where the detectors are working or partly working. One will thus find a lower number $\mathrm{N}(\mathrm{Z}^0)$ than the one used in the previous calculation of the branching ratio. Consequently a higher value of $Br(\mathrm{B}^- \to \mathrm{D}^0_\mathrm{J}(\mathrm{D}^{*+}\pi^-)\ell^-\bar{\nu}_\ell)$ would be measured. A careful study of this effect is necessary to complete the analysis.

8 Conclusion and outlook

As expected, the signal of D^{*+} was seen very clearly in the data. A signal of 16 events of narrow orbitally excited D-mesons, D^0_J, is also seen, and the branching ratio was measured to be

$$Br(B^- \to D^0_J(D^{*+}\pi^-)\ell^-\bar{\nu}_\ell) = \underline{(1.6 \pm 0.9)\,\%}$$

The upper limit of the branching ratio was estimated to

$$Br(B^- \to D^0_J(D^{*+}\pi^-)\ell^-\bar{\nu}_\ell) < \underline{3.0\,\%,\ (95\%\ \text{C.L.})}$$

However, Figure 24 makes one think that a further reduction of the background should be possible to give a more precise measurement of the branching ratio. This has proved to be more time consuming than this Cand. Scient. thesis gives room for. A complete analysis would also need to take care of the effect discussed in section 7.2. The present results must thus be taken as preliminary.

The analysis could in principle rather easily be extended to study the decay mode with $D^+ \to K^-\pi^+\pi^+$ in the final state. The number of charged pions is the same as in the present analysis (section 3.1), the difference is the presence of a π^0 or a γ as shown on page 14.

References

[1] Blatt, F. J., *Modern Physics*, McGraw-Hill, Inc., 1992

[2] Halzen, F. & Martin, A. D., *Quarks & Leptons: An Introductory Course in Modern Particle Physics.*, John Wiley & Sons, Inc., 1984

[3] Mandl, F. & Shaw, G., *Quantum Field Theory.*, John Wiley & Sons, Ltd., 1993

[4] Martin, B. R. & Shaw, G., *Particle Physics*, John Wiley & Sons, Ltd., 1994

[5] Kittel, C. & Kroemer, H., *Thermal Physics*, W.H. Freeman and Company, 1980

[6] Merzbacher, E., *Quantum Mechanics*, John Wiley & Sons, Inc., 1970

[7] Particle Data Group, Particles and fields, Part 1: Review of Particle Physics, *Physical Review D*, Vol. 54, July 1994

[8] Isgur, N. & Wise, M. B., Weak Decays of Heavy Mesons in the Static Quark Approximation. *Physics Letters B*, Vol. 232, p. 113, 1989

[9] Isgur, N. & Wise, M. B., Weak Transition Form Factors between Heavy Mesons. *Physics Letters B*, Vol. 237, p. 527, 1990

[10] Neubert, M., B Decays and CP Violation. CERN-TH/96-55. *International Journal of Modern Physics A* Vol. 11 p. 4173, 1996

[11] Neubert, M., Heavy Quark Masses, Mixing Angles, and Spin-Flavour Symmetry. CERN-TH.7225/94. *Proceedings S Raby and T Walker World Scientific.* Singapore. p. 125, 1994

[12] Isgur, N. & Wise, M. B., Spectroscopy with Heavy-Quark Symmetry. *Physical Review Letters*, Vol. 66, p. 1130, 1991

[13] Ming-Lu, Wise, M. B. & Isgur, N., Heavy-quark symmetry and $D_1(2420) \longrightarrow D^*\pi$ decay. *Physical Review D*, Vol. 45, p. 1553, 1992

[14] DELPHI Collaboration, Borisov, G., Di Ciaccio, L., Fischer, P-A, Simonetto, F., A Study of Orbitally Excited Charm Mesons in B Semileptonic Decays. DELPHI 96-102 CONF 31, 1996

[15] ALEPH Collaboration, Production of Orbitally Excited Charm Mesons in Semileptonic B Decays. *Zeitschrift für Physik* C73, p. 601, 1996

[16] OPAL Collaboration, A Study of Charm Meson Production in Semileptonic B Decays. *Zeitschrift für Physik* C67, p. 57, 1995

[17] ARGUS Collaboration, Observation of the $D^{*0}(2459)$ in $e^+ e^-$ annihilation. *Physics Letters B*, Vol. 221, p. 422, 1989;

ARGUS Collaboration, Resonance Decomposition of the $D^*(2420)^0$ through a Decay Angular Analysis. *Physics Letters B*, Vol. 232, p. 398, 1989;

Tagged Photon Spectrometer Collaboration, Observation of Excited Charmed Mesons. *Physical Review Letters*, Vol.62, p. 1717, 1989;

CLEO Collaboration, P-wave Charmed Mesons in $e^+ e^-$ annihilation. *Physical Review D*, Vol. 41, p. 774, 1990;

Tagged Photon Spectrometer Collaboration, Measurement of the Masses and Widths of L=1 Charmed Mesons. *Physical Review Letters*, Vol.72, p. 324, 1994;

CLEO II Collaboration, Production and Decay of $D_1(2420)^0$ and $D_2^*(2460)^0$. *Physics Letters B*, Vol. 331, p. 236, 1994

[18] ARGUS Collaboration, Observation of the Charged Isospin Partner of the $D^*(2459)^0$. *Physics Letters B*, Vol. 231, p. 208, 1989;

Tagged Photon Spectrometer Collaboration, Measurement of the Masses and Widths of L=1 Charmed Mesons. *Physical Review Letters*, Vol.72, p. 324, 1994;

CLEO II Collaboration, Observation of $D_1(2420)^+$ and $D_2^*(2460)^+$. *Physics Letters B*, Vol. 340, p. 194, 1994

[19] Godfrey, S. & Isgur, N., Mesons in relativized quark model with chromodynamics. *Physical Review D*, Vol. 32, p. 189, 1985;

Godfrey, S. & Kokoski, R., Properties of P-wave Mesons with One Heavy Quark. *Physical Review D*, Vol. 43, p. 1679, 1991;

Kaidalov, A. B. & Nogteva, A. V., Predictions of the Model of Quark Gluon Strings for Boson Masses and Widths. Systems Consisting of Light and Heavy Quarks. *Soviet Journal of Nuclear Physics*, Vol. 47, p. 321, 1988;

Rosner, J., P-wave Mesons with One Heavy Quark. *Comments on Nuclear and Particle Physics*, Vol. 16, p. 109, 1986

[20] Kreuter, C. J., 1997. *Measurements of* $\bar{B} \to D^{**} l^- \bar{\nu}$, DELPHI 97-64 PHYS 712

[21] DELPHI Collaboration, Performance of the DELPHI Detector, *Nuclear Instruments & Methods in Physics Research (Section A)* Vol. 378, p.. 57, 1996

[22] Leo, W. R., *Techniques for Nuclear and Particle Physics Experiments*, Springer-Verlag, 1994

[23] Kreuter, C. J., *Electron Identification using a Neural Network*, DELPHI 96-169 PHYS 658, 1996

[24] Sjøstrand, T., PYTHIA 5.7 and JETSET 7.4 Physics and Manual, *Computer Physics Communications*, Vol. 82, p. 74, 1994

[25] Perevoztchikov, V. & Smirnov, N., 1997. *PHDST Package Description* [online]. CERN. Available from: http://wwwcn.cern.ch/~nsmirnov/ phdst.html [Accessed 17 Nov 1997]

[26] Smirnov, N. & Spassoff, Tz., 1997. *SKELANA skeleton analysis program* [online]. CERN. Available from: http://wwwcn.cern.ch/~spassoff / skelana.html [Accessed 17 Nov 1997]

[27] Borgland, A. W. & Eigen, G., Kinematic Analysis Language - A User Manual, DELPHI 97-61 PROG 220

[28] Ekman, T. & Eriksson, G., *Programmering i Fortran 77*, Universitetsforlaget AS, 1981

[29] DELPHI Analysis Software Task Groups, 1997. *DST Analysis Libraries Writeup* [online]. CERN. Available from: http://wwwcn.cern.ch/~pubxx/tasks/doc/dstana/manual/dstana/dstana.html [Accessed 17 Nov 1997]

[30] Lyons, L., *Statistics for nuclear and particle physics*, Cambridge University Press, 1986

[31] Bock, R. K., *Breit-Wigner Distribution* [online]. CERN. Available from: http://www.cern.ch/RD11/rkb/AN13pp/node23.html#SECTION0002300000000000000000 [Accessed 12 Jan 1998]

A Distributions and statistics

In order to determine the mean and variance of a distribution various functions can be fitted to the given distribution. Breit-Wigner and Gaussian functions have been used in the present analysis.

A.1 Gaussian distribution

The Gaussian probability density function is given by

$$\mathrm{F}(x) = \frac{1}{\sigma\sqrt{2\pi}} \exp[-(x-\mu)^2/2\sigma^2] \tag{1}$$

where μ is the mean and σ^2 is the variance of the distribution.

The importance of the Gaussian distribution comes from the *central limit theorem* which states that [7]:

> If a continuous random variable x is distributed according to any probability density function with finite mean and variance, then the sample mean, $\bar{x}_n$, of n observations of x will have a probability density function that approaches a Gaussian as n increases.

A.2 Breit-Wigner distribution

The Breit-Wigner distribution is often used to describe particle resonant states and is given by

$$\mathrm{F}(x) = \frac{\Gamma/2\pi}{(x-x_0)^2 + \Gamma^2/4} \tag{2}$$

x_0 is the position of the maximum of the distribution (the distribution is symmetric around this maximum) and Γ is the width of the distribution [31].

A.3 The method of maximum likelihood

The method of maximum likelihood consists of finding the set of values for the given parameters which maximizes the joint probability density for all the data [7], and thus find the best estimate of the parameter.

The likelihood equation is

$$\frac{\partial \ln \mathcal{L}}{\partial \alpha_n} = 0 \tag{3}$$

where $\mathcal{L}$ is called the likelihood and $\boldsymbol{\alpha}$ is the set of parameters. Then [7]

If an efficient estimate $\hat{\boldsymbol{\alpha}}$ of $\boldsymbol{\alpha}$ exists, the likelihood equation will have a unique solution equal to $\hat{\boldsymbol{\alpha}}$.

A.4 χ^2 distribution

If $x_1, x_2, ..., x_n$ are independent Gaussian distributed random variables, then the sum $z = \sum^n (x_i - \mu_i)^2/\sigma_i^2$ is distributed as a χ^2 with n degrees of freedom [7].

The confidence level is obtained by integrating the tail of a function $f(z;n)$:

$$\mathrm{CL}(\chi^2) = \int_{\chi^2}^{\infty} f(z;n)\, dz \tag{4}$$

This is useful in order to evaluate the consistency of data with a model. The CL is the probability that a random repeat of the given experiment would observe a greater χ^2, when the model is assumed correct. It is also useful for confidence intervals for statistical estimators [7].